UNIVERSITY OF TURKU

Computational Investigation of Mechanical properties in multi-materials produced by Additive Manufacturing

Master's thesis

Materials Engineering Faculty of Technology

Department of Mechanical and Materials Engineering

Author

Aatif Imran

Supervisors

Associate Prof. Milica Todorovic

Dr. Mohsen Amraei

26.05.2025

Turku

Master's thesis

Subject: Materials Engineering

Author: Aatif Imran

Title: Computational Investigation of Mechanical properties in multi-materials produced by Additive Manufacturing

Supervisors: Associate Professor Milica Todorovic & Dr. Mohsen Amraei

Number of pages: 85

Date: 26.05.2025

Abstract

This thesis presents a comprehensive computational investigation into the mechanical behavior of multi-material components fabricated by Wire Arc Additive Manufacturing (WAAM). The study focuses on the combination of two widely used materials—ER70S-6 (a high-strength carbon steel) and SS316L (a corrosion-resistant stainless steel)—to explore the influence of stacking sequence, material interfaces, and transition zones on the tensile properties of bimetallic structures. Finite Element Analysis (FEA) simulations were conducted using Abaqus to evaluate force-displacement and stress-strain responses of both single-material and multi-material specimens.

Nine different multi-material specimens were modeled with varying material stacking configurations, with and without transition zones. The simulations revealed that symmetric stacking with strategically placed transition layers significantly enhances tensile performance by promoting uniform stress distribution and delaying fracture initiation. Specimens with abrupt or asymmetric interfaces exhibited higher stress concentrations, leading to premature failure. Fracture typically initiated near interface regions, highlighting the critical role of interfacial design in structural integrity. The study also established a robust simulation workflow on CSC Puhti, enabling high-performance computation for complex WAAM geometries. The results provide valuable insights into optimizing material arrangements for tailored mechanical behavior in additive manufacturing. This research lays the foundation for future experimental validation and advanced modeling of functionally graded materials, residual stress, and fatigue behavior in multi-material WAAM components.

Key words: Additive Manufacturing, Wire Arc Additive Manufacturing, Finite element analysis, multi-material, computational study, high performance computing, Stainless steel, high carbon steel.

Acknowledgement

I would like to express my heartfelt gratitude to Professor Antti Salminen for welcoming me into the *Digital Manufacturing and Surface Engineering (DMS)* group in the summer of 2024 and giving me the opportunity to work on Wire Arc Additive Manufacturing (WAAM) technology.

I am especially thankful to Associate Professor Milica Todorović for supervising this thesis. Her invaluable guidance, continuous support, and insightful mentorship were instrumental in every stage of this work. I also extend my sincere appreciation to my co-supervisor, Dr. Mohsen Amraei (University Teacher at UTU), whose unwavering support, constructive feedback, and deep expertise played a key role in shaping my understanding of Finite Element Modelling. From the very beginning, both supervisors have greatly helped me develop my scientific writing and critical thinking skills.

I am also grateful to Emilia Palo (University Teacher at UTU) for her guidance and active support throughout my master's studies, especially during the planning and execution of this thesis. A special thanks goes to Mr. Shafi Uddin, PhD researcher in the DMS group, for his generous assistance in helping me understand and work with WAAM. His support was invaluable to the success of this research.

I sincerely thank all my classmates and friends for fostering a positive and encouraging environment. In particular, I would like to acknowledge Abdul Malik, Nouman Qureshi, Ahmed Saleem, and Talha Saeed Ahmed for their constant encouragement. Finally, I am deeply grateful to my family for their unconditional love, support, and motivation throughout this journey.

Table of Contents

List of Figures

Nomenclature

Symbols:	Explanation:
σ	Stress
ε	Strain
ε^t	True Strain
σ^t	True stress
E	Youngs Modulus
σy	Yield Strength
σu	Ultimate strength
σf	Fracture strength
εu	Ultimate strain
εy	Strain at yeild
εf	Fracture strain
Fu/Fy or σu/ σy	Fracture strain capacity
εu/ εy	Ductility

Abbreviation:	Explanation
AM	Additive Manufacturing
DED	Direct Energy Deposition
WAAM	Wire Arc Additive Manufacturing
CAD	Computer Aided Design

ISO	International System Organization
FEA	Finite Element Analysis
FEM	Finite Element Modellin
FGM	Functionally Graded Materials
SS	Stainless steel
BM	Bimetallic
UTS	Ultimate Tensile strength
PBF	Powder bed fusion
BJ	binder jetting
SLM	Selective laser melting
SL	Sheet lamination
EBM	Electron beam melting
GMAW	Gas metal Arc Welding
PAW	Plasma Arc Welding
HPC	High performance computing

1 Introduction:

Additive Manufacturing (AM) is a technology that produces three-dimensional (3D) components directly from digital models by building them layer by layer. This process typically involves the deposition of polymers, ceramics, or metallic materials in successive layers. AM has gained widespread adoption across the global manufacturing industry due to its capability to produce large-scale parts with high deposition efficiency. Metal-based additive manufacturing processes are generally classified into four main categories: sheet lamination, powder bed fusion, binder jetting, and directed energy deposition [1]. The recent introduction of metal additive manufacturing into the construction industry has attracted significant attention from architects and structural engineers. Among the various techniques, wire-arc directed energy deposition (DED) commonly known as wire-arc additive manufacturing (WAAM) utilizes traditional welding processes combined with advanced robotics to fabricate components layer by layer. Unlike other metal 3D printing methods, WAAM is particularly advantageous for producing large-scale structures efficiently and cost-effectively, making it a promising solution for structural engineering applications [2] Directed Energy Deposition (DED), as defined by the ISO/ASTM 52900 standard, is an additive manufacturing (AM) process that utilizes concentrated thermal energy—such as an electric arc—to melt filler wire and build components. In this study, the process is specifically referred to as DED-ARC. This technique offers a competitive manufacturing solution for producing end-use parts that require high stiffness-to-mass ratios, complex and large-scale geometries, and are suited to low production volumes. One of the key advantages of DED-ARC is its wide material compatibility, as virtually any weldable metal can be processed. Moreover, integrating a welding torch with a robotic system allows for the fabrication of parts with minimal size constraints. With its ability to efficiently produce large, complex, and multifunctional structural components, DED-ARC is rapidly becoming a practical and appealing solution across various industries, including aerospace, automotive, marine, energy, defense, and other high-performance engineering sectors [3].

Multi-material 3D printing, particularly in WAAM, is gaining significant attention due to its ability to combine materials with different mechanical, thermal, and corrosion properties within a single component [4]. This approach allows for tailored performance, where specific regions of a structure can be optimized for strength, wear resistance, flexibility, or corrosion resistance. It also enables the fabrication of functionally graded materials (FGMs), improving overall component efficiency by

reducing weight while maintaining mechanical integrity [5]. In industries like aerospace, automotive, and marine, multi-material WAAM is particularly valuable for manufacturing lightweight, high-strength, and corrosion-resistant components at reduced costs compared to traditional multi-part assembly methods [6]. Combining ER70S-6 and SS316LSi enables the fabrication of functionally graded material (FGM) structures with tailored mechanical properties—such as enhanced strength, ductility, and corrosion resistance—that are unattainable using either material on its own. Their integration in WAAM processes presents a compelling solution due to the complementary nature of their properties, offering a balance of performance, cost-efficiency, and printability. This makes the ER70S-6 and SS316LSi pairing particularly suitable for industrial applications that demand both structural integrity and corrosion resistance without compromising on affordability or manufacturing flexibility [6].

The ability to layer different materials in WAAM provides several advantages as it improved Mechanical Properties – Combining materials with different strength and ductility characteristics enhances structural integrity, Optimized Cost and Performance – High-performance materials can be used only where needed, reducing material costs while maintaining functional requirements, Corrosion and Wear Resistance – Multi-material structures can have corrosion-resistant outer layers (e.g., SS316L) and high-strength inner layers (e.g., ER70S-6) for durability, Repair and Reinforcement Applications – Multi-material deposition enables in-situ repair of worn-out parts, extending their lifespan, Reduction in Post-Processing – Unlike traditional manufacturing, multi-material WAAM eliminates the need for complex joining techniques (e.g., welding or bolting).

Over the past several years, numerous researchers in the engineering field have employed finite element method (FEM)–based numerical simulations to investigate the behavior of the WAAM process [7], [3], [8], [9]. Engineering research has been conducted to present a comprehensive design study of the WAAM process using a finite element method (FEM) computational model, with a particular focus on evaluating the process capabilities for manufacturing complex components. The study specifically investigated the influence of inter-pass temperature on the thermal and structural behavior of the fabricated part [10]. In parallel, research efforts have also focused on optimizing the computational efficiency of WAAM simulations, emphasizing the significance of using finite element analysis (FEA) to model the WAAM process in a time-effective

manner. These studies underline the need for balancing simulation accuracy with reduced computational time to enable practical and scalable modeling approaches [7].

The high deposition rate of WAAM enables the rapid and flexible fabrication of complex metal components. However, this same flexibility can lead to significant thermal gradients within the workpiece, often resulting in distortion. To address this, the application of Finite Element Method (FEM) has become increasingly essential for predicting distortion levels and residual stresses in WAAM-produced parts. Incorporating FEM simulations into the pre-manufacturing phase allows for the optimization of process parameters and build strategies, reducing the need for costly physical trials and enhancing overall process reliability [8]. Advanced numerical simulations using FEM software have been conducted to investigate distortion behavior and assess the impact of cooling time between successive layer depositions in the WAAM process. These simulations provide valuable insight into how thermal cycles influence residual stresses and deformation, enabling more accurate prediction and control of the final component geometry [11]. Distortion prediction in the WAAM process has been carried out using numerical computational modeling, allowing for the analysis of thermal and mechanical responses during fabrication. This approach enables early identification of potential deformation issues and supports the development of optimized process strategies to minimize distortion in the final component [12]. A thermo-mechanical modeling study of the WAAM process was performed using commercial simulation software to analyze a semi-finished component. The investigation focused on the effects of wire feed speed and resulting temperature distribution during deposition. The findings revealed that the orientation and positioning of the deposited beads significantly influenced both the thermal profile and the final geometry of the component, highlighting the importance of deposition strategy in achieving dimensional accuracy and structural integrity [13].

1.1 Background of the thesis:

Conventionally, metal components have been manufactured through methods such as machining, casting and forging. However, these processes often involve extensive material removal and are increasingly unable to meet the growing demands for cost-efficiency, sustainability, and environmental responsibility in modern manufacturing. As a result, Additive Manufacturing (AM) has emerged as a key technology for producing custom-made metal components with reduced waste

and improved design flexibility. Out of different AM techniques, Wire Arc Additive Manufacturing (WAAM) stands out for its ability to fabricate large, low-volume metal parts efficiently, thanks to its huge deposition rate and adaptability [7], [14], [15]. However, the non-uniform expansion and contraction of material during the thermal cycles inherent to the WAAM process lead to the development of residual stresses and distortions within the fabricated component [14]. In large-scale WAAM processes, controlling residual stress and distortions is critically important to ensure dimensional accuracy and structural integrity. Drawing from the field of welding, several mitigation techniques have been developed to address these challenges, including pre-bending, thermal tensioning, and mechanical tensioning. These methods aim to balance or relieve internal stresses during fabrication and can be effectively adapted to WAAM to reduce deformation in large and complex components [16].

To identify optimal control strategies for managing residual stress and distortion, Finite Element (FE) modeling is widely employed. The most common approach involves sequentially coupled transient FE models that incorporate a moving heat source and simulate material deposition using the element birth technique. While this method offers high accuracy, the transient nature of the simulation combined with the nonlinear behavior of materials leads to extensive computational demands. As a result, these models are typically limited to small-scale components. When dealing with large-scale WAAM structures—often spanning several meters the conventional transient FE approach becomes impractical. Therefore, a more computationally efficient modeling method is required to enable rapid and reliable estimation of residual stresses and distortions in large WAAM builds [17]. An alternative approach employs a steady-state model using a Eulerian frame attached to the welding torch, allowing the material to “flow” through the finite element mesh. This formulation enables the thermal problem to be solved in a single time step, significantly reducing computational effort compared to conventional transient models. However, in many cases, the mechanical simulation remains time-dependent and is still solved using a transient approach, which continues to demand substantial computational resources. To further improve efficiency, the mechanical response can be approximated using static analyses, offering a practical solution for reducing simulation time while still capturing the essential effects of residual stress and distortion [7].

The prevailing literature on WAAM of stainless steels and ER70S6 specifically focuses on thermal and mechanical properties experimentally. Several research and review papers have examined the finite element analysis of austenitic stainless steel manufactured through WAAM but there are very few which focused on FEA of multi-material WAAM. Figure 1 shows the rising interest in FEA of WAAM over the years in the scientific community, suggests that research in this domain is still in its initial stages. By searching for keywords “Finite element analysis” and “wire arc additive manufacturing” in Scopus, in total 64 documents were received showing an increase in trend in recent years.

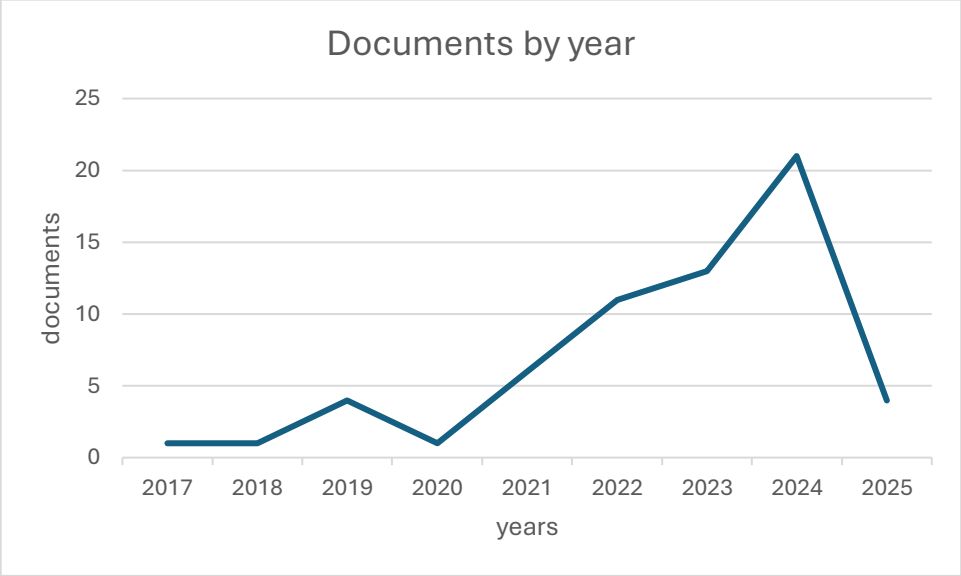

Figure 1 The publication trend of articles retrieved from the Scopus database using the keywords "finite element analysis" and "Wire arc additive manufacturing"

WAAM of multi-material is gaining significant attention due to its ability to combine materials with different mechanical, thermal, and corrosion properties in a single component, enabling the creation of functionally optimized structures. The ability to layer different materials allows for enhanced mechanical performance, cost efficiency, and tailored material properties for specific applications. By strategically placing materials based on their strengths, WAAM reduces the reliance on traditional joining techniques like welding or bolting while minimizing material waste and post-processing requirements. The selection of SS316L and ER70S-6 for multi-material WAAM is based on their complementary properties. SS316L, a stainless steel, provides excellent corrosion resistance, high ductility, and superior weldability, making it suitable for the outer layers of

structure exposed to harsh environments. On the other hand, ER70S-6, a mild steel welding wire, offers higher strength, good stiffness, and cost-effectiveness, making it ideal as a core material for structural applications.

The combination of these two materials allows for an optimal balance of mechanical performance and corrosion resistance, making it beneficial for industries like aerospace, marine, and structural engineering. However, understanding the behavior of multi-material interfaces is crucial, as differences in thermal expansion, bonding strength, and mechanical properties may influence failure modes.

Finite Element Analysis (FEA) plays a crucial role in evaluating the mechanical response of multi-material components, especially in our case where experimental testing is costly, time-consuming, and challenging. In multi-material WAAM, factors such as stress distribution, interfacial bonding strength, and fracture mechanisms need to be analyzed to ensure structural reliability. Through FEA-based simulations in Abaqus (Abaqus modelling and simulations explained step by step in appendix), it becomes possible to predict stress-strain behavior, force-displacement responses, and potential failure zones before physical testing. This computational approach allows for optimization of layer thicknesses, material deposition strategies, and process parameters, reducing trial-and-error in experimental fabrication. Additionally, FEA provides insights into residual stresses and thermal effects, which are crucial in multi-material structures where differences in thermal expansion can lead to warping or delamination. By using FEA in WAAM research, engineers can develop robust multi-material structures with improved performance while minimizing manufacturing defects and inefficiencies.

1.2 Aim and research questions:

The aim of this thesis is to computationally investigate the mechanical properties of multi-material components fabricated using Wire Arc Additive Manufacturing (WAAM), specifically focusing on the combination of SS316L and ER70S-6. The study aims to develop and validate finite element models in Abaqus to analyze the stress-strain behavior, force-displacement characteristics, and fracture mechanisms of these materials in both single-material and multi-material configurations. By optimizing layer thicknesses and studying interfacial bonding effects, this research seeks to

provide a deeper understanding of the mechanical performance and failure behavior of multi-material WAAM components. Additionally, the thesis will explore the implementation of a simulation workflow on CSC Puhti, optimizing computational efficiency for large-scale finite element simulations.

This study addresses the following key research questions:

- How accurately can finite element simulations replicate the tensile behavior of SS316L and ER70S-6?
- How do stress-strain relationships and force-displacement responses compare between computational results and experimental data of individual material specimens?
- What is the effect of material stacking variation on the mechanical performance of multi-material WAAM specimens?
- How does the interface between SS316L and ER70S-6 influence stress distribution, fracture behavior, and overall strength?
- Which material exhibits early failure in a multi-material configuration, and what are the dominant failure mechanisms?
- What computational challenges arise in multi-material WAAM modeling, and how can the simulation workflow be optimized on CSC Puhti for efficient and accurate analysis?

These research questions guide the investigation into mechanical performance, failure analysis, and computational modeling of multi-material WAAM structures, contributing to the broader understanding of multi-material additive manufacturing applications.

1.3 Outline of the thesis:

The thesis begins with a comprehensive literature review that lays the groundwork for the study by discussing key concepts related to Additive Manufacturing, particularly focusing on Wire Arc Additive Manufacturing (WAAM). It explores the fundamentals of finite element analysis (FEA), as well as the mechanical behavior of the base materials used in this study: ER70S-6 and SS316L stainless steel. The review also highlights prior research on multi-material additive manufacturing

and identifies existing gaps, particularly in computational modelling of mechanical properties in bimetallic structures.

Following the literature review, the thesis moves into the computational phase, where individual material models for SS316L and ER70S-6 are developed using finite element simulations in Abaqus. These models are validated by comparing the simulation outputs with available experimental data, ensuring the accuracy of the stress-strain and force-displacement responses of each material. Once validated, the study progresses to modeling multi-material specimens, with various stacking configurations of ER70S-6 and SS316L. Both simple bimetallic models without transition layers and more complex specimens with thin interface zones are created to evaluate how interface design affects mechanical behavior.

The results of these simulations are analyzed in detail by examining stress-strain curves, force-displacement responses, and tensile properties such as ultimate tensile strength (UTS), ductility, and fracture strain. Particular attention is given to the role of the interface in transferring stress and delaying failure, as well as the effect of stacking symmetry and material arrangement. A comparative study of nine different multi-material specimens is conducted to identify which configurations exhibit optimal combinations of strength and ductility.

Finally, the thesis presents a detailed discussion of the findings, drawing conclusions about the influence of material sequencing and interface behavior on the overall performance of multi-material WAAM components. The study concludes by summarizing the key outcomes and contributions, while also recommending directions for future work, such as incorporating residual stress modeling, exploring functionally graded materials, and experimentally validating the computational results.

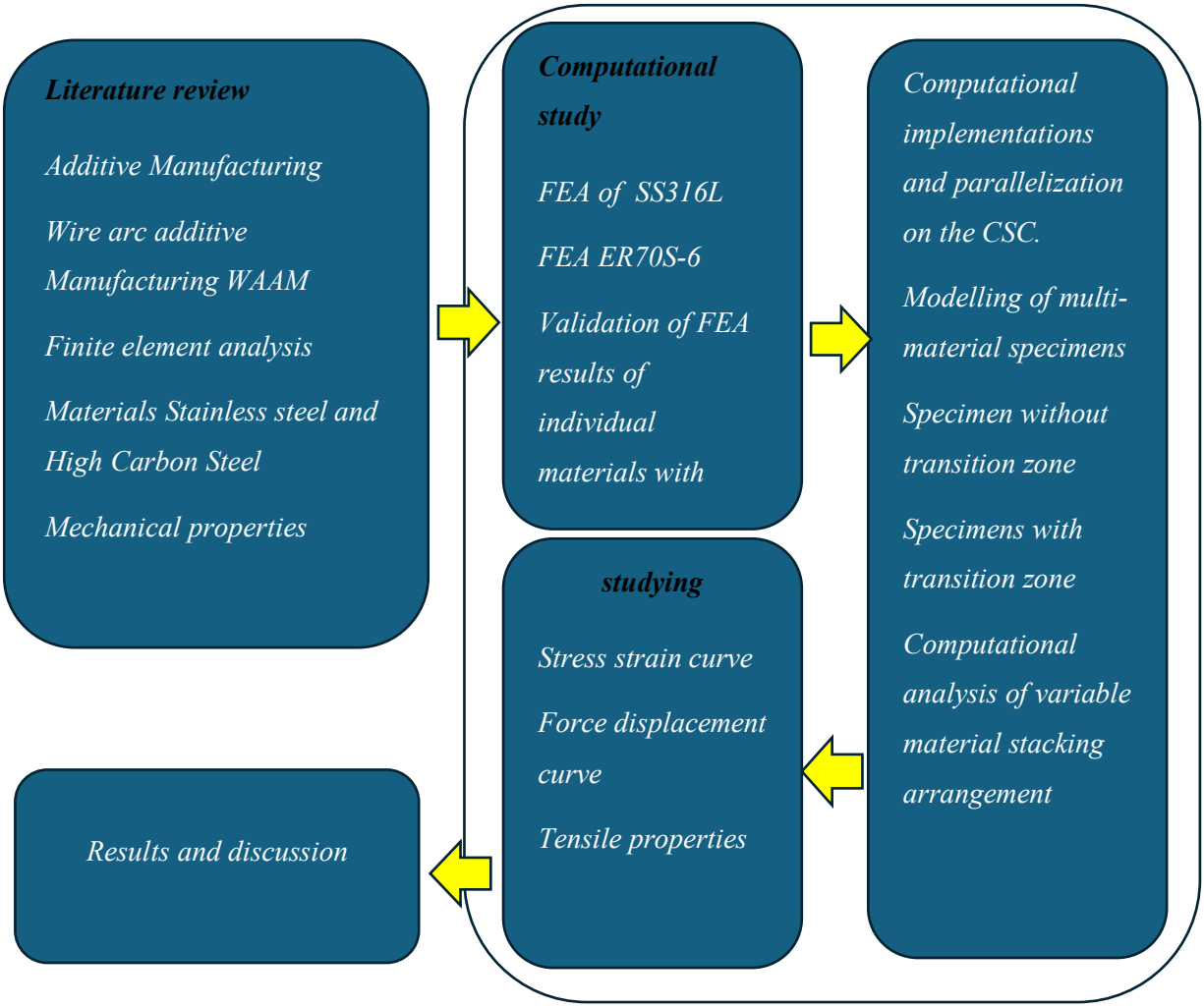

Figure 2 Research Plan for thesis

1.4 Declaration

I hereby declare that AI-based tools have been used during the preparation of this thesis to assist with sentence structure refinement and grammar correction. These tools were employed solely to enhance the clarity, coherence, and readability of the written content. All technical ideas, interpretations, analyses, and conclusions presented in this work are my own.

2 Literature review:

2.1 Additive manufacturing:

Additive Manufacturing (AM), also known as 3D printing, is a manufacturing process that creates components by layer-by-layer deposition of material, enabling the fabrication of complex geometries that are difficult or impossible to achieve with conventional subtractive methods [15]. Metal Additive Manufacturing (AM) encompasses several technologies that enable the fabrication of complex metallic components through layer-by-layer deposition. These processes vary in their energy sources, feedstock materials, and manufacturing applications. The most common metal AM techniques include Powder Bed Fusion (PBF), Directed Energy Deposition (DED), Binder Jetting (BJ), and Sheet Lamination (SL), each with distinct advantages and limitations [18].

Powder Bed Fusion (PBF) processes, such as Selective Laser Melting (SLM) and Electron Beam Melting (EBM), use a high-energy laser or electron beam to selectively melt and fuse metallic powder in a controlled atmosphere. SLM operates with a high-powered laser, making it ideal for high-precision applications such as aerospace and medical implants, but it requires inert gas environments to prevent oxidation. In contrast, EBM utilizes an electron beam under vacuum conditions, reducing residual stresses but with slightly lower resolution than SLM [19].

Directed Energy Deposition (DED) processes, including Laser Metal Deposition (LMD) and Wire Arc Additive Manufacturing (WAAM), use a directed energy source (laser, electron beam, or electric arc) to melt and deposit metal in the form of powder or wire. LMD employs a laser to melt powder as it is deposited, providing good precision but requiring extensive post-processing [20]. WAAM, which utilizes an electric arc and wire feedstock, is particularly suitable for large-scale metallic structures, offering high deposition rates and cost efficiency but lower resolution compared to PBF methods [19].

Binder Jetting (BJ) is a metal AM technique where a binding agent selectively bonds layers of metal powder, which are later sintered or infiltrated to achieve final mechanical properties. This process does not involve melting, allowing for high-speed production of complex geometries, but requires secondary sintering or infiltration steps to enhance mechanical strength [21].

Sheet Lamination techniques, such as Ultrasonic Additive Manufacturing (UAM), join thin metal sheets using ultrasonic vibrations and localized plastic deformation without melting the material. While UAM allows embedding of sensors and dissimilar materials, it is limited by the need for post-processing to achieve full density [2].

2.2 Wire Arc Additive Manufacturing:

Wire Arc Additive Manufacturing (WAAM), a directed energy deposition (DED) technique, utilizes an electric arc to melt metal wire feedstock, depositing it layer-by-layer to form near-net-shape components. Integrating arc welding principles with robotic automation, WAAM is adept at fabricating large-scale structures, as leveraged in this study for multi-material SS316L and ER70S-6 specimens. The process begins with a substrate (e.g., steel plate), where a welding torch—typically gas metal arc (GMAW) or plasma arc (PAW)—generates an arc between the wire tip and the substrate, melting the wire into a molten pool (Figure 6). The torch, guided by a robotic arm, follows a programmed path, solidifying each layer as it cools, with deposition rates ranging from 1–10 kg/h depending on wire diameter (typically 0.8–1.2 mm) and arc current (100–300 A) [22].

The WAAM system comprises a power source, wire feeder, and shielding gas (e.g., argon-CO_2 mix), ensuring stable arc formation and minimal oxidation (Figure 6). Multi-material capability is achieved by switching wire feedstock mid-process—e.g., transitioning from ER70S-6 to SS316L—enabling tailored properties like corrosion resistance atop high strength. Unlike powder-based methods, WAAM operates in an open environment, supporting large builds (up to meters in scale), though thermal cycles induce residual stresses (50–200 MPa) and distortions (0.5–2 mm/m), as reported in steel WAAM studies [13].

This process's mechanics—arc stability, layer stacking, and material transitions—directly influence the tensile properties under investigation here. Understanding these dynamics is essential for accurate FEA modeling in Abaqus, as explored later, making WAAM's operational principles foundational to this research.

2.3 Properties and applications of materials used:

2.3.1 Stainless steel:

SS316L is a low-carbon austenitic stainless steel, distinguished by its superior corrosion resistance, high ductility, and excellent mechanical properties, making it a preferred material for marine, biomedical, and aerospace applications [23]. Stainless steels, alloys primarily composed of iron, chromium (16-18%), and nickel (10-14%), form a protective oxide layer that enhances oxidation resistance and durability [13]. The low carbon content (≤0.03%) in SS316L minimizes carbide precipitation during welding, preventing intergranular corrosion and ensuring high-temperature stability [2]. Mechanically, SS316L has a yield strength of approximately 290 MPa and an ultimate tensile strength of around 550 MPa, making it moderately strong but highly ductile, with a fracture strain ranging from 45% to 60%. Compared to carbon steels like ER70S-6, SS316L has a lower stiffness (Young's modulus ~190 GPa) but greater toughness, allowing it to withstand impact and cyclic loading [19]. In tensile loading, SS316L exhibits a high degree of plasticity, allowing it to absorb energy before failure. The presence of nickel (Ni) and molybdenum (Mo) enhances its ability to withstand high temperatures, oxidation, and chloride-induced pitting corrosion. However, SS316L is softer compared to ER70S-6 and has lower stiffness, which may affect its compatibility in multi-material structures where high rigidity is needed. Their application include marine and offshore structures, where corrosion resistance is critical, aerospace components, due to its excellent strength-to-weight ratio and oxidation resistance, biomedical implants and surgical instruments, where biocompatibility is essential, food processing equipment, benefiting from its resistance to acidic and high-moisture environments, additive manufacturing, particularly in multi-material WAAM applications, where a balance of corrosion resistance and strength is required.

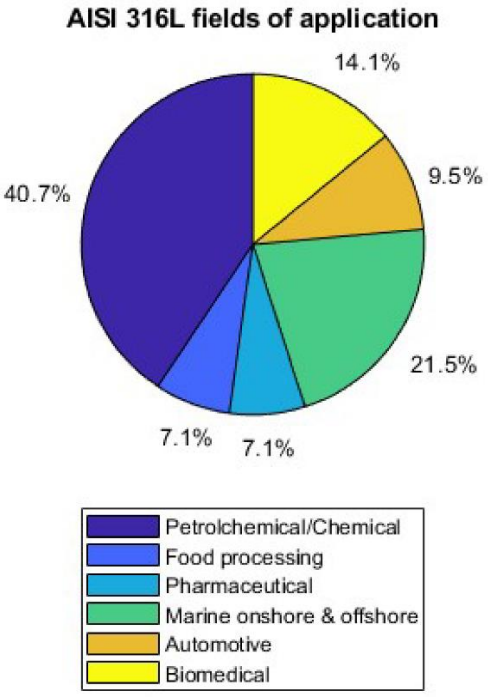

Figure 3 Fields of application of SS 316L [24]

2.3.2 ER70S-6

Each digit in the ER70S-6 classification carries specific information about the filler wire's characteristics. The prefix **'ER'** stands for *Electrode Rod*, indicating that the wire is suitable for TIG or MIG welding processes. The number **'70'** represents the minimum tensile strength of the deposited weld metal, expressed in ksi (70 ksi or approximately 483 MPa). The **'S'** denotes that the wire is a *solid* (non-flux-cored) wire. The final digit, **'6'**, specifies the wire's chemical composition, shielding gas compatibility, and recommended polarity, as defined by the ASME Section IIC, SFA 5.18 standard [25].

ER70S-6 is a low-carbon steel welding wire, widely used in gas metal arc welding (GMAW) and Wire Arc Additive Manufacturing (WAAM) due to its high strength, good ductility, and excellent weldability. Mild steel, classified as a carbon steel with a carbon content ranging from 0.05% to 0.32%, provides an optimal balance of mechanical strength and cost-effectiveness, making it ideal for structural applications, automotive frames, and heavy machinery components [19]. The presence of manganese (1.4-1.85%) and silicon (0.8-1.15%) in ER70S-6 enhances deoxidation, allowing for cleaner welds with fewer inclusions, which is particularly beneficial in WAAM layer deposition [18]. The yield strength of ER70S-6 ranges from 400 to 500 MPa, while the ultimate tensile

strength (UTS) lies between 480 and 600 MPa, making it suitable for load-bearing applications [2]. The material exhibits a moderate fracture strain (~25-30%), ensuring sufficient plastic deformation before failure, though it lacks the corrosion resistance of stainless steel. In multi-material WAAM applications, when paired with stainless steel SS316L, ER70S-6 serves as a strong base material, contributing to structural integrity and cost efficiency, but requires careful interface control to prevent galvanic corrosion and brittle interfacial failures [26]. In tensile loading, ER70S-6 undergoes elastic deformation up to its yield point (~400 MPa), followed by plastic deformation until failure. It has a moderate strain-hardening capacity, meaning it strengthens slightly before failure, but it is prone to brittle fracture under high strain rates. Its applications include structural steel components in buildings and bridges, heavy machinery parts that require high strength and good weldability, automotive applications, including chassis and frames, repair and maintenance of industrial equipment, wire Arc Additive Manufacturing (WAAM) applications, where cost-effective and high-strength materials are needed.

Table 1 Chemical composition of ER-SS316L and ER70S-6 wire (mass fraction/%) [27].

Element	Cr	Ni	Mo	Mn	Si	C	P	S	Fe
SS316-L	18.57	11.72	2.57	1.72	0.54	0.015	0.024	0.008	Bal.
ER70S-6	0.068	1.4	0.8	-	-	-	-	-	Bal.

The combination of ER70S-6 and SS316L in WAAM provides a promising balance of strength, ductility, and corrosion resistance. However, interface properties, stress distribution, and thermal expansion mismatches must be carefully analyzed to ensure structural integrity. The FEA simulations in this study aim to predict stress-strain behavior, fracture mechanisms, and failure modes to optimize the stacking strategy and enhance mechanical performance in multi-material WAAM applications. By understanding the interaction between these materials, this research contributes to the development of functionally graded structures, which can be applied in industries requiring lightweight, high-strength, and corrosion-resistant components. In multi-material WAAM, SS316L is often stacked over mild steel to provide an outer corrosion-resistant layer, ensuring durability in harsh environments while leveraging the strength of ER70S-6 as a core material [20]. However, joining SS316L and ER70S-6 presents challenges due to differences in thermal expansion

and the potential formation of brittle intermetallic phases, requiring careful process optimization to achieve a strong metallurgical bond [28].

2.4 Mechanical properties of materials:

Mechanical properties define a material's response to external forces, guiding the selection and design of engineering components. In the context of Wire Arc Additive Manufacturing (WAAM), these properties are critical due to the process's layer-by-layer deposition, which introduces thermal gradients, residual stresses, and potential anisotropy—factors that differentiate WAAM components from conventionally manufactured ones. Key mechanical properties include:

Strength: The ability of material to withstand applied forces without failure, critical for load bearing WAAM structures like those using ER70S-6. Standard unit used for measuring strength is Pa or Mpa [29].

Hardness: The ability of material to resist surface deformation or penetration. Hardness has no SI unit, its measured in scales such as Brinell, Rockwell, Vickers [30].

Ductility: Ability of material to undergo plastic deformation before breaking, vital for SS316L's toughness in multi-material applications. Percentage or strain (unitless) used for measuring ductility [31].

Toughness: Ability of material to absorb energy before fracturing, influencing failure resistance at material interfaces. Standard unit used for measuring toughness is J/m^3 [32].

Elasticity: Ability of material to return to its original shape after deformation. Standard unit used for measuring elasticity is Pa or GPa [33].

Plasticity: Ability of material to permanently deform under load, shaping the post-yield behavior in tensile loading. It has no standard unit [34].

Fracture Toughness: Ability of material resist crack propagation, particularly relevant at SS316L-ER70S-6 interfaces where thermal mismatch may initiate flaws. Standard unit used for measuring fracture toughness is MPa·√m [35].

Stiffness: Stiffness refers to a material's or structure's ability to resist deformation under applied forces such as bending, twisting, or stretching. It is primarily governed by the material's elastic modulus (also known as Young's modulus), which quantifies its tendency to return to its original shape after being deformed. A higher elastic modulus indicates a stiffer material. In multi-material designs, stiffness plays a key role in balancing rigidity and flexibility. The standard unit for measuring stiffness is newtons per meter (N/m) [36].

In WAAM, these properties are influenced by process parameters (e.g., heat input, cooling rates) and material interactions, especially in multi-material components where SS316L's corrosion resistance and ER70S-6's strength must be harmonized. For instance, residual stress from thermal cycles can reduce effective strength, while interfacial bonding affects toughness and fracture behavior—challenges that finite element analysis (FEA) in Abaqus aims to address in this study. Although all properties are relevant, this research focuses on tensile properties—strength, ductility, and elasticity—measured through stress-strain and force-displacement responses. These are pivotal for understanding how SS316L and ER70S-6 behave individually and in combination under tensile loading, particularly at interfaces where failure may initiate. Tensile testing, simulated computationally, thus forms the cornerstone of this investigation, as detailed in the following section.

2.5 Tensile properties of materials:

Tensile properties quantify a material's response to uniaxial loading, critical for assessing the mechanical performance of Wire Arc Additive Manufacturing (WAAM) components in this study. These properties, derived from stress-strain curves in tensile testing, are pivotal for validating finite element (FE) models of SS316L and ER70S-6, both individually and in multi-material configurations, using Abaqus. The key tensile properties relevant to this research include:

Young's Modulus, E (GPA): is a type of Elastic Modulus that measures the stiffness of a material under tensile and compressive forces. It exhibits the ratio of stress to strain in the linear elastic region of a material's stress-strain curve.

$$E = \boldsymbol{\sigma}/\varepsilon$$

where **σ** is stress and **ε** is strain [37].

For WAAM materials like SS316L and ER70S-6, with E ≈ 190–200 GPa, it governs initial deformation under load, essential for predicting force-displacement behavior.

Yield Strength σy (Mpa): The stress at which a material begins to undergo plastic deformation instead of elastic deformation is known as yield strength. The yield point in stress strain curve is a mid-point between elastic and plastic regions (Figure 4 '3'). Before this point curve is straight and in elastic region, after this point plastic regions begins, and material start to deform [38]. In WAAM, yield strength varies with deposition direction and thermal history, influencing the structural integrity of multi-material specimens [39].

Ultimate Tensile Strength UTS (Mpa): A material's ultimate tensile strength (UTS), also referred to simply as tensile strength, represents the maximum stress a material can withstand while being stretched or pulled before it breaks. It is the peak value on a stress-strain curve and marks the point just before complete failure occurs. UTS is a critical property for assessing how a material or component will perform under load, providing insight into its capacity to resist tension. This characteristic is essential for structural design and failure prediction (see Figure 4, points '1 & 2') [40]. UTS is a key metric for comparing single-material benchmarks to multi-material performance in this study.

True Stress (Pa) and True Strain (unitless):

True stress (σ^t) refers to the applied force divided by the cross-sectional area of a material at any given point during deformation. Unlike engineering stress, which is based on the material's original cross-sectional area, true stress accounts for the continuous reduction in area as the material stretches and thins under load. As deformation progresses, the decreasing area leads to an increase in true stress, making it a more accurate measure of the material's resistance to deformation. True stress offers a realistic representation of material behavior under tensile loading, especially beyond the yield point. While engineering stress data is typically obtained from tensile tests, it is often converted to true stress for accurate analysis.

$$\textbf{True Stress } (\sigma^t) = \sigma\,(1+\varepsilon)$$

where σ is engineering stresses and ε is engineering strain [41].

True strain (ε^t) quantifies the deformation or elongation of a material relative to its instantaneous length, rather than its original length. Unlike engineering strain, which is based on the initial dimensions, true strain continuously accounts for the material's changing length during deformation. It is calculated as the natural logarithm of the ratio between the current length and the original length. This approach provides a more accurate and continuous representation of the material's elongation, especially in cases of large or non-uniform deformation. True strain is particularly useful for analyzing material behavior beyond the elastic region

$$\textbf{True Strain } (\varepsilon^t) = \ln(1+\varepsilon)$$

where ε is engineering strain [41].

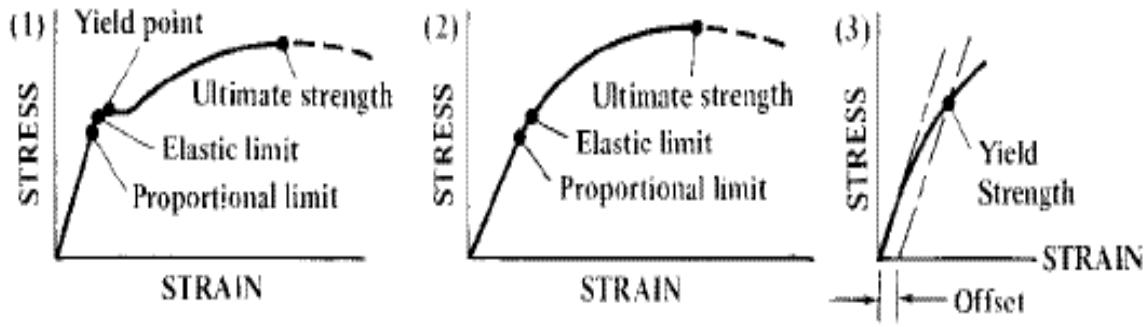

Figure 4 Understanding Stress strain curve [29].

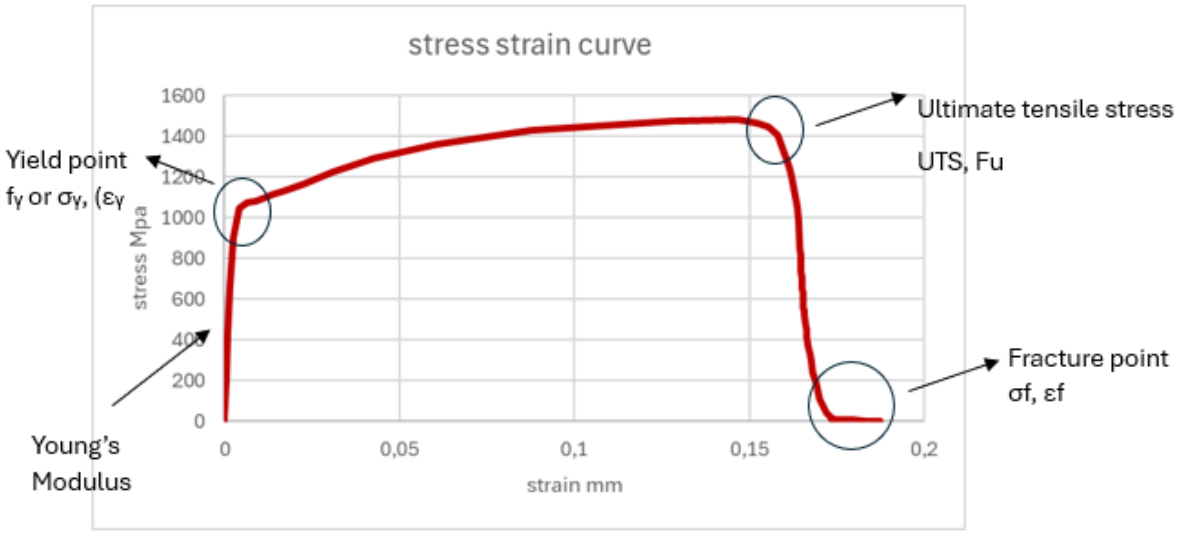

Figure 5 Indicating tensile properties from self-generated stress strain curve

In WAAM, tensile properties are influenced by process-induced factors such as residual stresses and anisotropy, which can alter stiffness, yield behavior, and failure modes—particularly at multi-material interfaces where thermal expansion mismatches between SS316L and ER70S-6 may concentrate stresses. This study leverages these properties to validate FE models against experimental data for single materials, then extends the analysis to multi-material specimens with varying layer arrangements. By simulating stress-strain and force-displacement responses, the research aims to identify optimal configurations and understand interfacial failure mechanisms, addressing the tensile behavior questions outlined earlier.

2.6 Computational Modeling in Additive Manufacturing

Finite Element Analysis (FEA) has become an indispensable tool for investigating the mechanical behavior of components produced by Wire Arc Additive Manufacturing (WAAM), a directed energy deposition (DED) process highlighted in this thesis for its high deposition rates and suitability for large-scale multi-material structures. As noted earlier, WAAM's thermal cycles induce residual stress and distortions, necessitating predictive modeling to optimize process parameters and material arrangements. Abaqus, a commercial FEA software, is widely employed in WAAM research due to its robust capabilities in simulating nonlinear material behavior, coupled thermal-mechanical interactions, and complex geometries—key aspects for analyzing tensile properties of SS316L and ER70S-6 in single and multi-material configurations, as pursued in this study.

Prior FEA studies on WAAM have primarily focused on single-material systems to establish simulation reliability. [14] utilized Abaqus to develop a thermo-mechanical model for WAAM of low-carbon steel (akin to ER70S-6), simulating residual stress and distortion in wall structures. Their model, incorporating a moving heat source and element birth technique, accurately predicted stress fields (within 12% of X-ray diffraction data), highlighting FEA's ability to capture deposition-induced effects. Similarly, [42] applied FEA to analyze the mechanical behavior of WAAM SS316L, focusing on thermal and stress evolution during deposition. Their simulations, validated against experimental data, showed good agreement in stress distribution, emphasizing the importance of process parameter optimization—a foundation for this thesis's validation phase.

For multi-material WAAM, which is central to this research, FEA studies have explored interfacial mechanics and mechanical performance. [43] used Abaqus to model a WAAM bimetallic structure transitioning from mild steel to stainless steel, simulating tensile loading to assess stress distribution across the interface. Their findings indicated that gradual material transitions reduced stress concentrations by up to 25% compared to abrupt interfaces, aligning with this study's aim to investigate SS316L-ER70S-6 arrangements. [44] further advanced this by simulating a steel-nickel alloy WAAM component in Abaqus, revealing interfacial weakening due to thermal mismatch—insights critical for predicting failure modes in multi-material tensile specimens here.

Abaqus's user-defined material (UMAT) is a custom material model that allows users to define their own constitutive behavior of a material using a Fortran subroutine. This is especially useful when the built-in material models in Abaqus do not accurately represent the material behavior being studied. This have further enhanced WAAM modeling precision. [45] implemented a UMAT to account for anisotropic tensile properties in WAAM ER70S-6, reflecting microstructural variations from arc deposition. Their simulations, validated with experimental data, showed a 10-15% yield strength increase along the deposition direction, informing this study's single-material modeling approach before multi-material extension. Additionally, researchers have addressed computational efficiency, a concern noted in this thesis background. Ding et al. [14] optimized Abaqus simulations by simplifying transient analyses, reducing computation time for large-scale WAAM parts—an approach this thesis adapts via CSC Puhti workflows.

Despite progress, FEA of multi-material WAAM remains underexplored, as this document's Scopus trend (Figure 1) suggests. Existing studies often assume perfect interfacial bonding, neglecting defects like porosity or lack-of-fusion common in WAAM [4], a limitation acknowledged in this study's scope. Moreover, while thermal effects are critical, many models simplify these, potentially underestimating residual stress impacts on tensile behaviour, a gap this research partially addresses through elastic-plastic modelling, though microstructural effects are excluded.

3 Methodology:

This chapter presents the computational methodology adopted to investigate the tensile behavior of multi-material components fabricated via Wire Arc Additive Manufacturing (WAAM), with a focus on SS316L and ER70S-6. The study primarily employs finite element analysis (FEA) in Abaqus to simulate uniaxial tensile tests, beginning with individual material modeling and subsequently extending to multi-material configurations with varied stacking arrangements. The simulation workflow is structured into distinct phases: material property definition, specimen design, FEA model setup, and post-processing. All simulations were executed on the CSC Puhti supercomputing platform to ensure computational efficiency and scalability.

The initial phase of the study involved modeling the tensile behavior of individual materials—SS316L and ER70S-6. To validate the reliability of the computational model, simulation results were compared with available experimental tensile test data. This step was critical to ensure that the material responses captured in the FEA matched the experimentally observed stress-strain and force-displacement behavior. The material models were built using input parameters derived from literature, including density, Young's modulus, Poisson's ratio, plastic stress-strain curves, as well as ductile damage initiation and damage evolution parameters. These inputs were essential for accurately simulating material nonlinearity and fracture behavior.

One limitation during this phase was the availability of experimental data: while tensile data was available for multi-material specimens, specific data for individual materials was limited. This posed a challenge in validating single-material simulations, as the available experimental curves were derived from composite specimens. Despite this, the comparison demonstrated good agreement in the elastic and plastic regions, validating the FEA model's credibility for both materials.

Following the validation of individual material models, the study progressed to simulating multi-material tensile specimens. These were designed with various stacking arrangements of SS316L and ER70S-6 within the gauge length to analyze how material configuration affects mechanical response. The objective was to explore the effect of interface placement, material orientation, and transition layers on the tensile behavior of the composite structure. Unlike the single-material simulations, direct experimental comparison for these configurations was not feasible due to a lack

of specimen-specific test data. Nevertheless, the study provides valuable predictive insights into stress distribution, fracture patterns, and material synergy in multi-material WAAM structures.

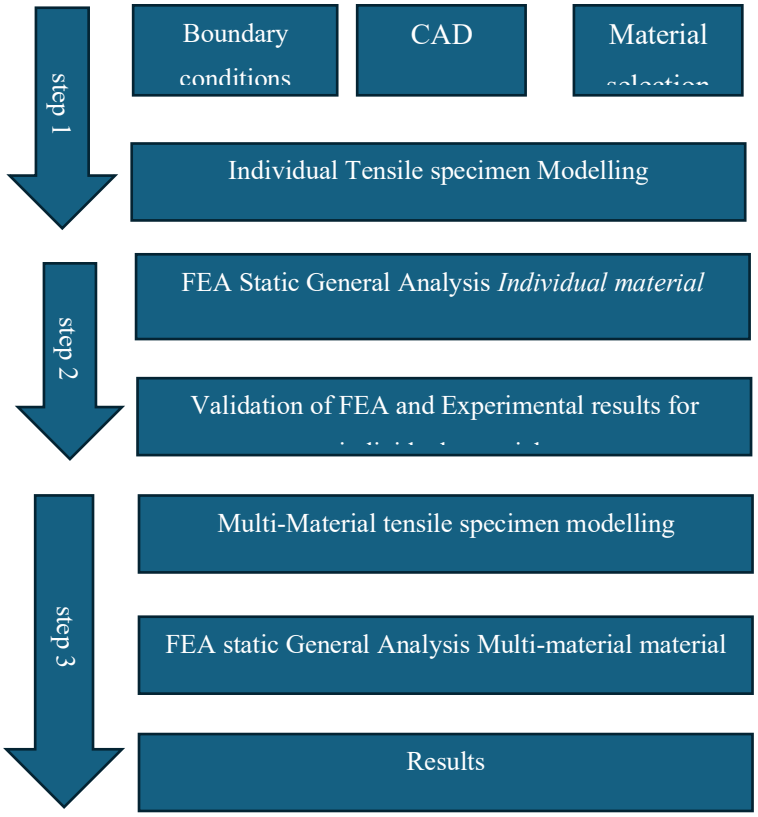

Figure 6 Adopted workflow for multi-material optimization and DED arc AM

3.1 Experimental setup:

The fabrication of multi-material tensile specimens was carried out using a Wire Arc Additive Manufacturing (WAAM) system, as illustrated in the first image. The setup includes a 6-axis robotic arm equipped with a GMAW welding torch, which enables automated and precise deposition of material layers. The robotic system is controlled via a dedicated control cabinet, while the welding process itself is powered by a welding machine capable of handling both ER70S-6 and SS316L feedstock wires. A filler wire spool continuously supplies material to the nozzle, where the arc is generated between the wire and the substrate. The working table, upon which the metal substrate is mounted, provides a stable base for deposition and allows for rotational movement if needed.

During the deposition process, the filler wire is melted by the electric arc and deposited layer by layer onto the substrate. Shielding gas is supplied through the nozzle to prevent oxidation and ensure a clean, defect-free weld pool. The robot follows a pre-programmed tool path to deposit successive layers of either ER70S-6 or SS316L in a controlled manner, enabling the creation of vertically built, multi-material walls. In the case of material transitions, the welding process is briefly paused, and the feedstock wire is manually switched to introduce a transition zone between the two materials. This zone is critical for promoting metallurgical bonding and reducing abrupt property mismatches.

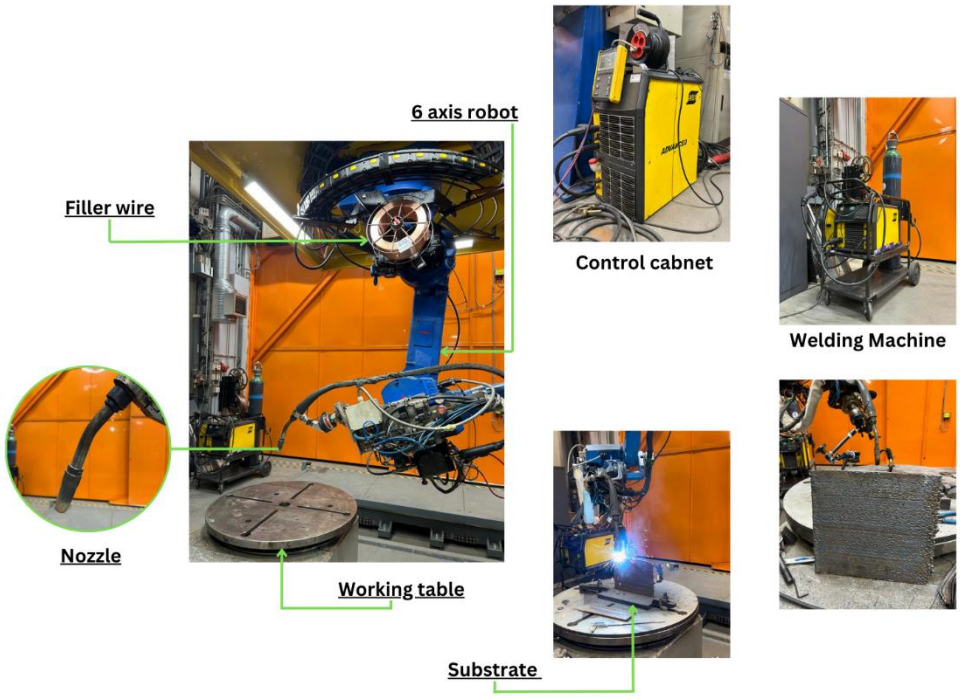

Figure 7 Experimental setup of WAAM at KTK Lab, UTU

Figure 6 shows a detail experimental set-up that is installed in UTU where WAAM experimentation is normally performed.

The second image provides a schematic representation of the printed wall structure, tensile specimen geometry, and corresponding simulation model. The structure comprises alternating layers of WAAM-deposited ER70S-6 (top, in blue) and SS316L (bottom, in yellow), separated by a narrow transition region (highlighted in green). The tensile specimens were extracted from this bi-material wall, with the gauge length (32 mm) positioned to encompass the transition region to

investigate interfacial behavior. The simulation model replicates this configuration to analyze stress distribution, damage evolution, and fracture behavior under tensile loading.

Together, these figures demonstrate the complete workflow from material deposition to tensile specimen design, emphasizing the importance of controlled stacking, interface placement, and WAAM process stability in achieving reliable mechanical performance in multi-material components.

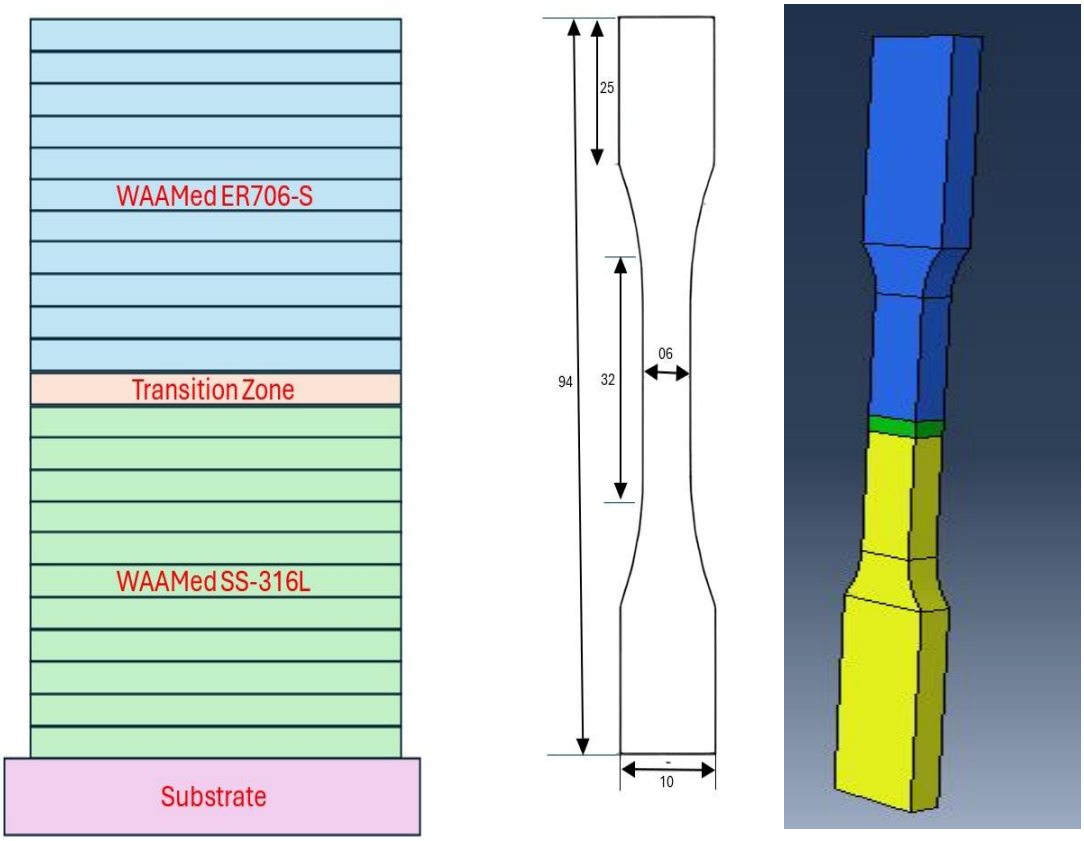

Figure 8 Schematic representation of WAAMed multimaterial part, specimen dimension and 3D model

3.2 Computational setup:

The computational modeling in this study was conducted using Abaqus/CAE and Abaqus/Standard, a powerful finite element analysis (FEA) platform widely used in engineering and research. Abaqus was selected due to its robust capabilities for nonlinear simulations, especially in capturing large deformation, plasticity, and damage evolution—all of which are critical for accurately modeling the fracture behavior of WAAM-fabricated multi-material structures. Its built-in support for ductile damage models, coupled with user-friendly preprocessing tools and solver stability, made it a

suitable choice for simulating the complex mechanical response of bimetallic specimens under tensile loading.

To analyze the mechanical behavior of the WAAM-fabricated multi-material specimens, a detailed finite element modeling approach was employed using Abaqus CAE. The simulations aimed to replicate the tensile testing process under uniaxial loading and to capture critical mechanical responses such as stress distribution, plastic deformation, and fracture behavior. The computational setup involved defining accurate geometry, assigning material properties, setting boundary conditions, and implementing damage mechanics to simulate failure initiation and propagation.

Each tensile specimen was modeled in 3D using deformable solid elements with a refined mesh in the gauge region to ensure accurate stress and strain predictions. Separate material sections were assigned for ER70S-6 and SS316L, with a transition zone introduced to replicate the interface between materials. The elastic-plastic material behavior was defined using experimentally informed stress-strain data, and advanced material models incorporating ductile damage initiation and evolution were applied to predict fracture. Key input parameters included density, Young's modulus, Poisson's ratio, true plastic stress-strain curves, damage initiation criteria, and damage evolution laws.

Boundary conditions were applied by fixing one end of the specimen and applying a displacement-controlled load at the other end to simulate tensile loading. A symmetric approach was followed wherever applicable to reduce computational effort without compromising accuracy. The general static step in Abaqus was used with nonlinear geometry enabled to account for large deformation effects.

All simulations were performed on the CSC Puhti supercomputer, leveraging parallel computing resources to handle the computational demand, especially for multi-material models with complex interfaces. The use of high-performance computing significantly reduced the simulation time and allowed for batch processing of all nine stacking configurations. The output data, including reaction forces, displacements, and damage evolution, were post-processed to extract force-displacement and stress-strain curves, which were then used for comparative analysis across all specimen types.

In total, two individual material specimens—one of ER70S-6 and one of SS316L—were modeled and simulated to validate the tensile behavior of each material against available experimental data.

For these validation models, simple rectangular specimens were created to replicate standard tensile test conditions. The simulation results for both materials, including stress-strain and force-displacement curves, were compared with experimental data (as shown in Figure 8) to confirm the accuracy of the finite element model and material definitions used in Abaqus.

Once the individual material models were validated, the study was extended to include nine multi-material specimens, each with a unique stacking arrangement of ER70S-6 and SS316L within the gauge length. These configurations were designed to explore how different material distributions, symmetry, and transition zones affect the mechanical response under uniaxial tensile loading. The models included both sharp and gradual transitions between materials, allowing for an in-depth investigation of stress concentration zones and fracture initiation at the interfaces. Each configuration was subjected to the same loading conditions and meshing strategy to ensure consistency across the simulations and to enable direct comparison of results.

3.3 Individual materials:

A 12 mm block with 3mm thickness has been modelled for tensile testing and mechanical properties of SS316L and ER70S-6. These FEA results were compared with experimental results to validate. Simulations were conducted in Abaqus/Standard (version 2022) using a static, general solver. 3D solid models were meshed with C3D8R elements, refined near interfaces (element size ~0.5 mm) for accuracy. Material models used elastic-plastic behavior with isotropic hardening, incorporating ductile damage initiation based on equivalent plastic strain and damage evolution via linear softening, with parameters. Boundary conditions fixed one end, with the other displaced at 0.002 s^{-1}, executed on CSC Puhti for efficiency.

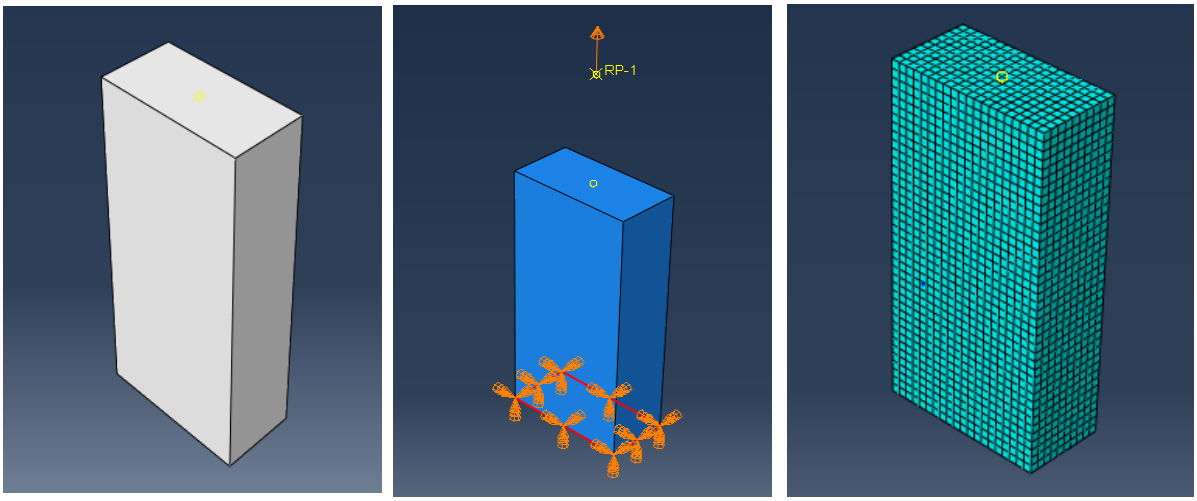

Figure 9 Individual specimen modelling

3.4 Multi-materials:

The objective is to investigate the mechanical properties of multi-material WAAM components, specifically SS316L and ER70S-6, under tensile loading. This setup extends from validated single-material models, aiming to predict stress distribution, force-displacement responses, and failure mechanisms in configurations like abrupt, layered, and graded transitions. The process is critical for understanding interfacial effects and optimizing multi-material designs, addressing research questions on stress concentration and failure behavior.

The multi-material tensile specimens are designed based on ASTM E8 standards, with dimensions of 32 mm gauge length, 6 mm width, and 3 mm thickness can be seen in figure 7, adapted for WAAM's layer-by-layer deposition. The arrangements modeled include:

Abrupt Transition: A sharp interface at the mid-length of the gauge, simulating a sudden change from SS316L to ER70S-6 (Figure 9).

Graded Configuration: A gradual transition reflecting functionally graded material (FGM) concepts to reduce stress concentrations.

The 3D geometry is created in Abaqus, meshed using 8-node linear brick elements (C3D8R) for their robustness in capturing nonlinear behavior. The mesh is refined near interfaces to an element size of approximately 0.3 mm and in gauge area it is 0.5m to accurately capture stress

concentrations, while coarser elements (2 mm) are used in regions with lower stress gradients to optimize computational efficiency.

As an initial trial, a simple bi-material specimen was modeled with ER70S-6 stacked directly on top of SS316L, without introducing any intermediate or transition layer. This configuration was used to identify stress concentration zones and observe the fracture mechanism under abrupt material transition.

As illustrated in Figure 9, the simulation of the specimen without a transition zone revealed a pronounced stress concentration at the material interface, acting as a weak point that led to premature failure. This outcome highlighted the critical role of the transition zone in enabling a smoother stress transfer between materials with differing mechanical properties. The transition region mitigates abrupt stiffness changes and helps reduce localized stress peaks at the interface.

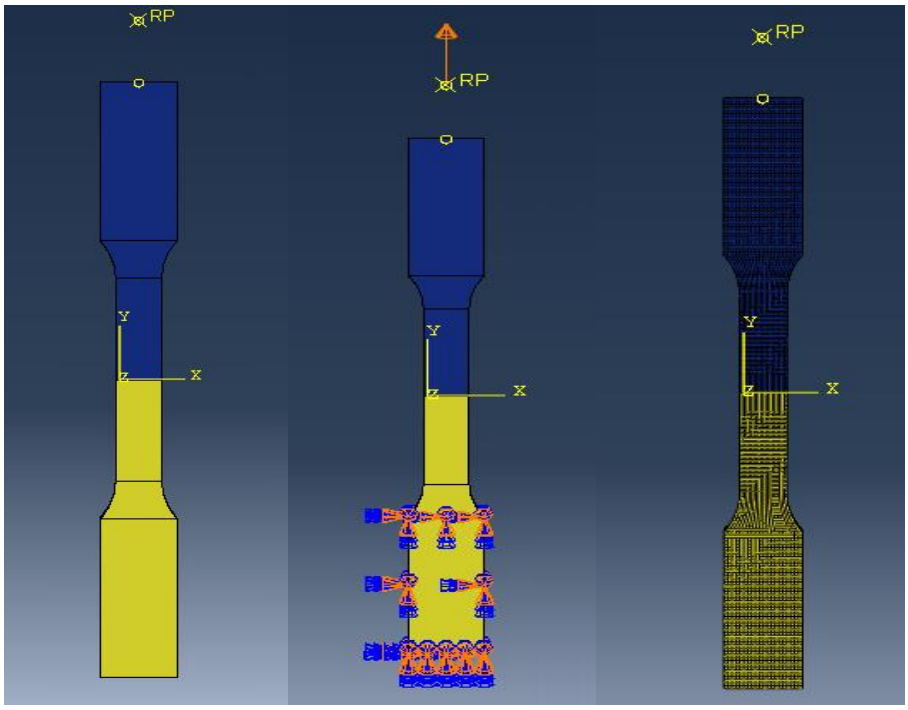

Figure 10 Tensile specimen without transition zone

In response to these findings, the study proceeded to develop and simulate nine different multi-material stacking configurations, each incorporating varied layering sequences and, in some cases, transition zones. These configurations were developed to systematically investigate how material

stacking sequence, interface behavior, and material distribution affect the tensile performance of WAAM-fabricated multi-material components. The design of the specimens was carefully structured to include variations in the number of layers, placement of transition zones, and material combinations, all within a consistent gauge length of 32 mm.

Some specimens, such as Specimen 7, consist of a simple two-material configuration, where ER70S-6 and SS316L each occupy 15 mm of the gauge length, with a 2 mm thick transition zone in between. The reason certain configurations appear as pairs under the same number (e.g., Specimen 7) is because they are mirror images of each other—the material stacking order is reversed, but the structure and dimensions are otherwise identical. These mirrored pairs help assess the impact of vertical material orientation on tensile behavior.

Specimens 1 and 2 involve a three-layer arrangement, with each layer approximately 10 mm thick and separated by 1 mm transition zones. Specimens 3 and 4 also feature three layers, but in some cases, like Specimen 3, the same material (e.g., SS316L) appears in adjacent layers. While this might visually suggest a two-layer structure, it is in fact a three-layer specimen—only the adjacent layers are composed of the same material.

Specimens 5, 6, 8, and 9 are designed with four layers, each approximately 7.25 mm thick, along with three 1 mm transition zones to maintain the total 32 mm gauge length. In configurations where two or more adjacent layers use the same material such as in Specimens 6, 8, and 9—the transition zones between these similar layers are effectively merged into the same material, eliminating any mechanical discontinuity at those interfaces.

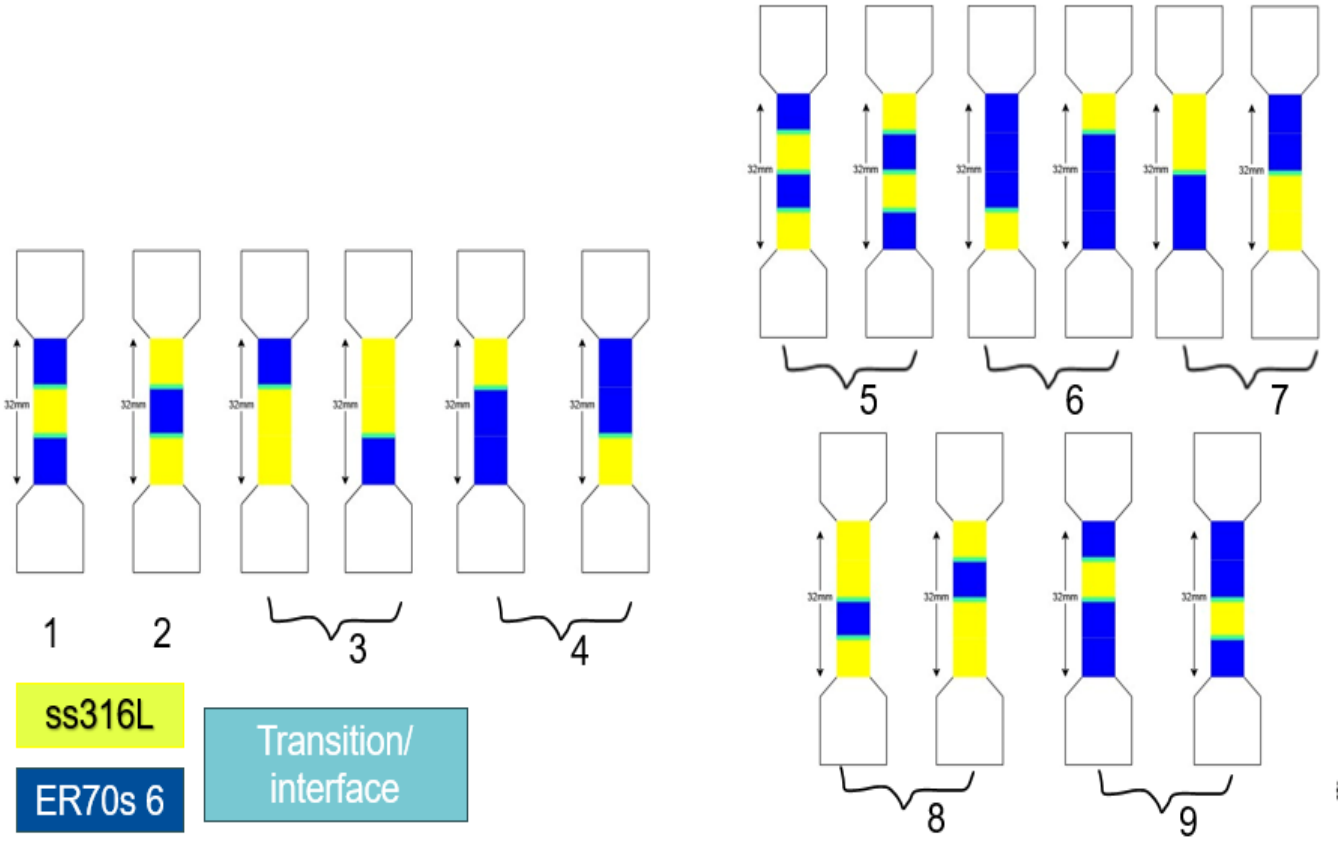

Figure 11 9 specimens with different stacking of materials

Both SS316L and ER70S-6 are modeled using elastic-plastic material models with isotropic hardening, reflecting their nonlinear behavior under tensile loading. The material properties, sourced from literature and summarized in Table:

Table 2 Mechanical properties of ER70S6, SS316L & Transition zone used as Input in Abaqus

Material	young modulus (Mpa)	poison ratio	yield strength (Mpa)	ultimate tensile strength (Mpa)	fracture strain	stress triaxiality	strain rate	displacement at failure
ER70S-6	210000	0.3	400-500	480-600	0.34	1.2	1	0.136

SS316-L	190000	0.3	270-300	550-620	0.35	1.2	1	0.144
Transition zone	200000	0.3	360	500-550	0.36	1.2	1	0.14

True stress and true strain are calculated from engineering values to account for large deformations, using the equations $\sigma^t = \sigma(1 + \varepsilon)$ and $\varepsilon^t = \ln(1 + \varepsilon)$, ensuring accuracy in the plastic region.

To simulate failure, a ductile damage model is implemented, with damage initiation based on equivalent plastic strain and damage evolution following a linear softening law. The parameters for damage initiation and evolution are derived from literature, acknowledging the challenge of limited experimental data for WAAM-specific conditions. This approach allows for predicting crack initiation and propagation, particularly at interfaces, enhancing the model's ability to capture failure mechanisms.

The tensile test simulation is set up to replicate experimental conditions. One end of the specimen is fully constrained (all displacements U1, U2, U3 set to zero), while the other end is subjected to a displacement of 15 mm-20mm, corresponding to a strain rate of approximately 0.002 s^{-1}. This loading rate is chosen to match typical experimental tensile testing protocols, ensuring comparability with validation data.

The simulations are conducted using Abaqus/Standard (version 2022) with a static, general solver, focusing on the mechanical behavior under room temperature conditions post-manufacturing. The multi-material setup involves assigning different materials to regions within the model, achieved by defining material sections or element sets. For instance, the abrupt transition model assigns SS316L to one half and ER70S-6 to the other, while the graded configuration uses a spatially varying material property field to simulate the transition.

The interface between SS316L and ER70S-6 is assumed to have perfect bonding, meaning no relative motion or separation is allowed, simplifying the contact definition. This assumption is made to focus on mechanical behavior, recognizing that real-world interfaces may exhibit defects or incomplete bonding due to WAAM's thermal cycles

3.5 Development of Platform/Environment for Abaqus Simulations on CSC Puhti

CSC Puhti is a high-performance computing (HPC) cluster that offers significant advantages for running computationally intensive Abaqus simulations. Using Puhti instead of a local Abaqus installation provides enhanced computational power, reducing simulation times and enabling larger, more complex analyses. HPC systems like Puhti are designed for parallel processing, allowing users to leverage multiple CPU cores and greater memory resources efficiently. Compared to local machines, these resources help achieve higher accuracy and faster execution. This section explores the computational benefits of using Puhti, including resource allocation, CPU usage, and overall efficiency in running Abaqus simulations.

The implementation of Abaqus on CSC Puhti requires users to first establish access by creating an account and logging into the system via a secure shell (SSH) connection. Once access is granted, the Abaqus module must be loaded using the command module load abaqus/2022, which ensures that the appropriate version of the software is available for execution. Unlike local installations, Puhti relies on the Slurm job scheduler for managing computational workloads. Users must prepare a batch script specifying key parameters such as the number of CPU cores, memory allocation, and execution commands for Abaqus. An example batch script is provided in figure 11 to illustrate best practices for resource allocation. Once a job is submitted, it runs in the background, and its progress can be monitored remotely. Upon completion, the results are retrieved from Puhti for further post-processing and analysis.

```
#!/bin/bash
#SBATCH --job-name=Job-xxxxx.inp
#SBATCH --error=%j.err
#SBATCH --output=%j.out
#SBATCH --nodes=x # x=1,2,3,4,....
#SBATCH --ntasks-per-node=x # x equal to or less then 40
#SBATCH --time=05:00:00
#SBATCH --mem-per-cpu=4g
#SBATCH --partition=large
#SBATCH --account=project_xxxxx
unset SLURM_GTIDS
module purge
module load abaqus/2022
###cd /users/mtodorov/Aatif/test_node
cd /scratch/project_2001978/Aatif_Imran/waam_simulation/specimens
echo $TMPDIR
echo $SLURM_NTASKS
# env-file ++++++++++++++++++++++++++++++++++++
if [[ -f abaqus_v6.env ]]; then
    mv abaqus_v6.env abaqus_v6.env_previous
fi
# FOR ABAQUS RUNS ON > 1 NODE, MPI IMPLEMENTATION  IS IMPI !
echo "mp_mpi_implementation = IMPI" >> abaqus_v6.env
echo "mp_rsh_command = 'ssh -n -l %U %H %C'" >> abaqus_v6.env
NODE_LIST=$(scontrol show hostname ${SLURM_NODELIST} | sort -u)
mp_host_list="["
for host in ${NODE_LIST}; do
    mp_host_list="${mp_host_list}['$host', ${SLURM_CPUS_ON_NODE}],"
done
mp_host_list=$(echo ${mp_host_list} | sed -e "s/,$/]/")
echo "mp_host_list=${mp_host_list}"  >> abaqus_v6.env
echo $SLURM_NTASKS
# env-file ++++++++++++++++++++++++++++++++++++
abq2022 job=xxxxx-results input=Job-xxxx.inp cpus=$SLURM_NTASKS scratch=$TMPDIR -interactive -verbose

```

Figure 12 script for CSC Puhti simulations

This SLURM batch script is designed to submit and execute an Abaqus job on a high-performance computing (HPC) cluster using the 2022 version of Abaqus. It specifies resource allocation (e.g., number of nodes, tasks per node, memory, partition, and wall time), loads necessary modules, sets up the working directory, and prepares the environment file (abaqus_v6.env) with MPI configuration for parallel processing across multiple nodes using IMPI. It dynamically generates a list of hostnames for MPI execution and launches the Abaqus simulation with the specified input file, utilizing all allocated CPU tasks and storing intermediate files in the scratch directory for improved performance.

A comparative analysis of CSC Puhti and a local Abaqus installation provides valuable insights into the computational efficiency of HPC resources. A primary performance metric is computation time, where Puhti demonstrates superior capabilities by executing simulations significantly faster than a local workstation. The extent of performance improvement depends on factors such as the number

of CPU cores utilized and the memory allocated to the simulation. Additionally, CPU and memory utilization play a crucial role in determining the efficiency of Abaqus simulations. By leveraging multiple processing cores and allocating sufficient memory, Puhti optimizes computational performance and minimizes execution time.

Another important consideration is the scalability of simulations. The ability to increase the number of CPUs directly impacts computational efficiency and solution accuracy. While additional processing power generally leads to reduced simulation times, it is essential to assess the diminishing returns associated with excessive parallelization. Furthermore, managing disk space is critical, particularly for large output files such as. odb result files.

3.6 Limitation of the study

While this study offers meaningful insights into the mechanical behavior of multi-material components produced via Wire Arc Additive Manufacturing (WAAM), there are certain limitations that must be acknowledged.

The finite element models (FEA) developed in Abaqus are based on simplified assumptions regarding material homogeneity, perfect bonding at interfaces, and uniform material deposition. These assumptions may not fully replicate the complex, real-world conditions inherent to the WAAM process. Factors such as thermal effects, residual stresses, and microstructural variations that naturally arise during additive manufacturing are not explicitly incorporated into the simulations, which may influence the accuracy of the predicted mechanical responses.

Moreover, the adopted elastic-plastic material models provide a general representation of mechanical behavior but may fall short in capturing detailed damage evolution, phase transformations, or anisotropic behavior often observed in WAAM-fabricated structures. Specifically, the interface between SS316L and ER70S-6 is assumed to exhibit perfect metallurgical bonding. However, in practical scenarios, this interface may be subject to incomplete diffusion, micro-defects, or intermetallic compound formation, all of which could significantly impact mechanical integrity and fracture behavior.

Additionally, the study primarily utilizes literature-based experimental data for validation purposes. While this approach is useful for benchmarking, it may introduce discrepancies due to variations in material sourcing, processing parameters, and testing standards used in other studies. This could potentially affect the consistency and direct comparability of the results.

Finally, the scope of mechanical evaluation in this research is limited to tensile testing. Other important performance aspects such as fatigue resistance, impact behavior, and thermal stability remain unexplored. Likewise, the influence of key WAAM process parameters—including deposition speed, heat input, and cooling rate—on the final mechanical properties has not been explicitly investigated. These aspects represent important directions for future research to enable a more comprehensive understanding of multi-material WAAM performance.

4 Results and discussion:

4.1 Mesh sensitivity Analysis

Mesh sensitivity analysis was conducted to ensure the accuracy and numerical stability of the finite element simulations while optimizing computational cost and resource utilization. In finite element modeling, mesh density directly influences the resolution of stress and strain gradients, especially in regions experiencing high deformation such as the gauge section and material transition zones. A coarser mesh may reduce simulation time but can result in inaccurate predictions, while an unnecessarily fine mesh increases computation time without significant gains in accuracy. Hence, performing a mesh sensitivity study is a critical step to strike the right balance between solution accuracy and computational efficiency.

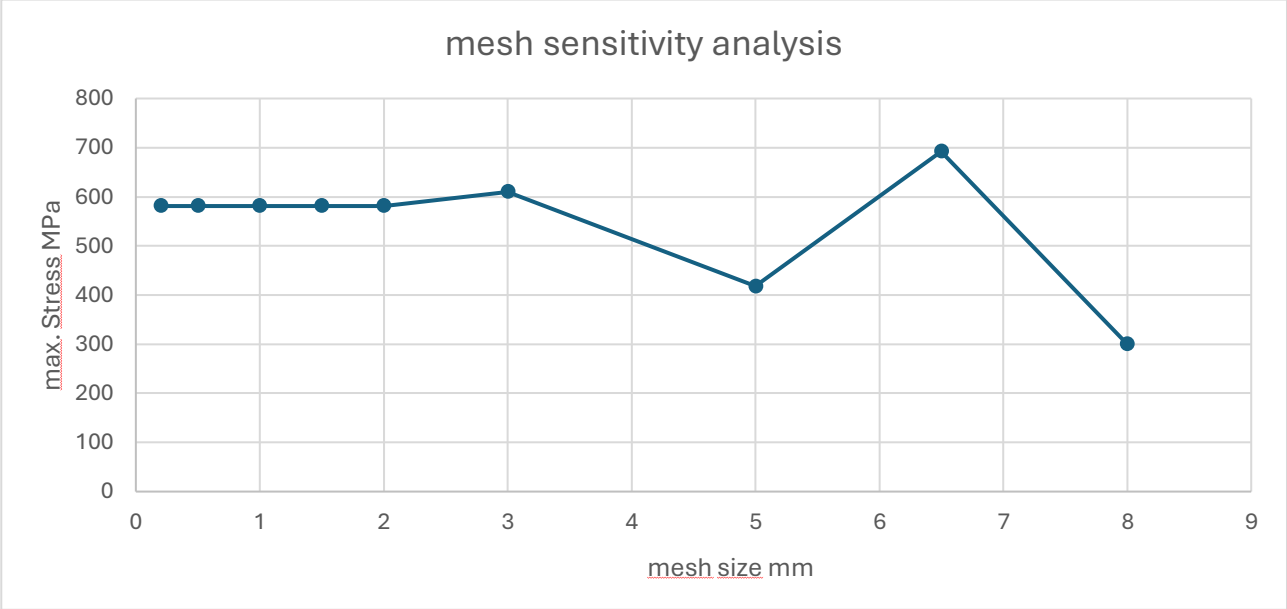

Figure 13 Mesh sensitivity analysis

To perform this analysis, a series of simulations were run using progressively refined mesh sizes applied to a representative single-material tensile specimen. The primary evaluation metric was the maximum stress value recorded in each simulation. A comparison plot of mesh size versus maximum stress (Figure 12) was generated to assess the convergence behavior. As the mesh was

refined, the changes in stress values began to diminish, indicating that the solution was approaching a mesh-independent result.

The results indicated that convergence began at a mesh size of approximately 3 mm, with further refinement producing only marginal changes in maximum stress values. Based on this trend, a mesh size of 0.5 mm was selected for the gauge region of the multi-material specimens to ensure accurate stress-strain predictions, particularly around the onset of yielding and necking.

Furthermore, a finer mesh of 0.3 mm was applied specifically in the transition zones between ER70S-6 and SS316L, where stress concentrations and localized deformation were anticipated due to material mismatch. This localized mesh refinement allowed better resolution of interface behavior, which was critical for capturing damage initiation and fracture propagation in the multi-material configurations.

4.2 Individual Material Modeling and Simulations:

4.2.1 ER70S-6

The mechanical and tensile properties of the ER70S-6 WAAM (Wire Arc Additive Manufactured) specimen were analyzed using finite element analysis (FEA) and experimentally validated. For this analysis, a rectangular block of 12 mm height, 6 mm width, and 3 mm thickness were modeled and subjected to uniaxial tensile testing in Abaqus to investigate its stress-strain behavior, force-displacement response, fracture and failure characteristics, damage evolution, and plastic strain displacement.

Figure 1 presents the Von Mises stress distribution in the ER70S-6 block under tensile loading conditions. The stress concentration regions are evident, highlighting the localized deformation zones and the onset of failure. The transition from elastic to plastic deformation is clearly observed, with maximum stress localized at the

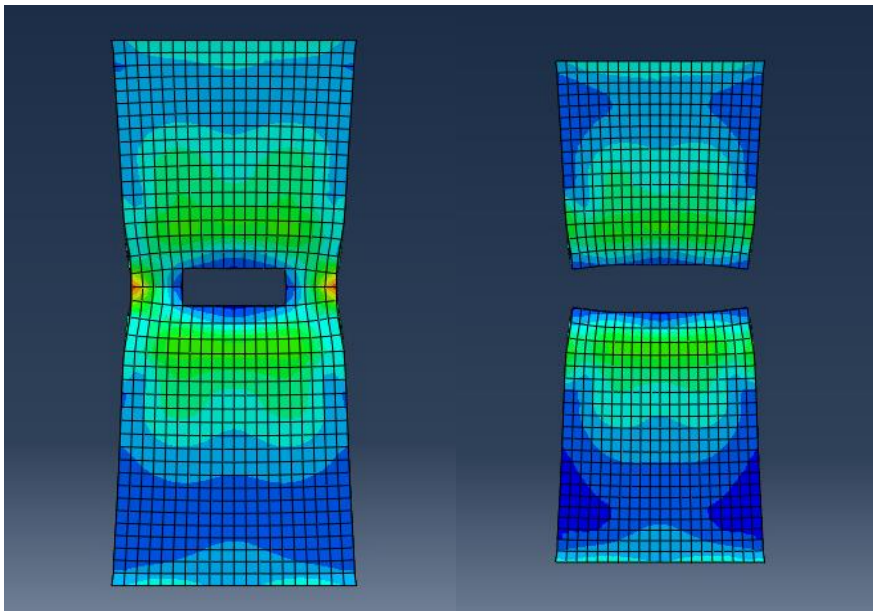

Figure 14 ER70S-6 specimen simulations result

Figures 2 and 3 compare the force-displacement and stress-strain curves obtained from FEA simulations with experimental data. The force-displacement curve (Figure 2) illustrates that the simulated response closely follows the experimental trend, capturing the initial elastic behavior, yield point, strain hardening region, and post-necking softening behavior. A similar correlation is observed in the stress-strain curve (Figure 3), where the ultimate tensile strength (UTS), yield stress, and strain-hardening characteristics are well represented in the FEA results.

The damage modeling results confirm that the failure behavior is accurately captured in the simulation. The element deletion approach was employed to model material degradation and crack propagation. Figure 4 displays the fracture process in the ER70S-6 specimen, showing a progressive failure mechanism that corresponds well with the experimental fracture behavior.

The comparative evaluation of FEA and experimental results demonstrates a high level of agreement in predicting the mechanical properties of ER70S-6 WAAMed specimens. The slight deviations observed in the post-UTS region could be attributed to material anisotropy, microstructural inhomogeneities, or simplifications in the constitutive damage model. Nevertheless,

the overall correlation between the numerical and experimental data validates the reliability of the FEA approach in replicating the tensile behavior of ER70S-6.

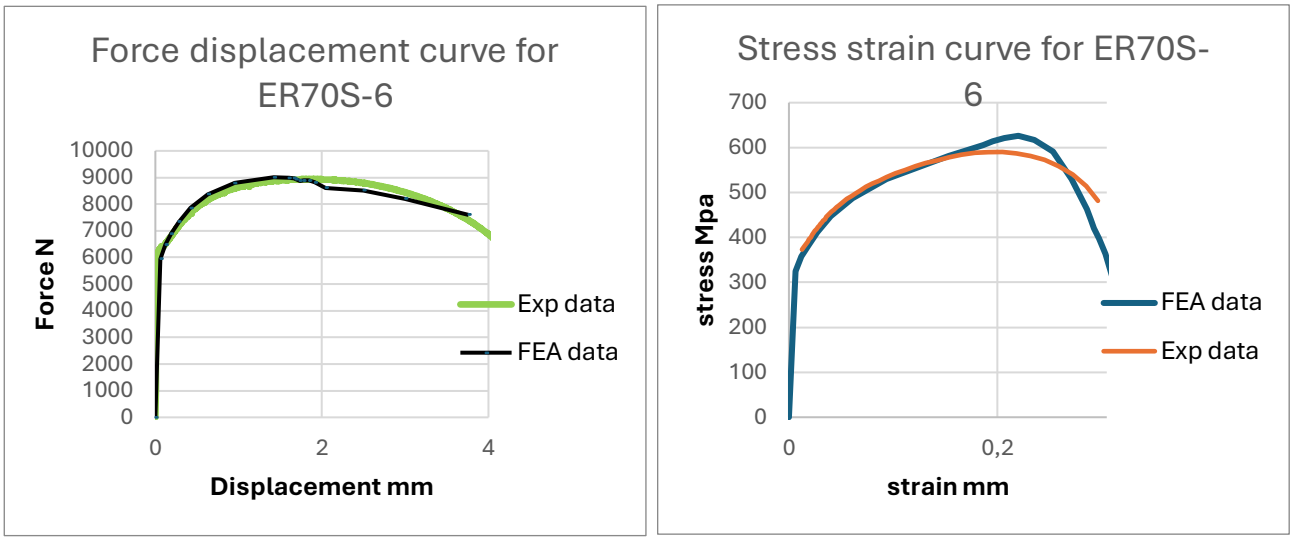

Figure 15 Force displacement curve and stress strain curve of ER70S 6

4.2.2 SS316L:

For the stainless steel **SS316L** specimen, tensile testing was simulated in Abaqus to assess its stress-strain response, force-displacement behavior, and fracture characteristics. The finite element analysis (FEA) results were compared with experimental data to validate the model and ensure accurate representation of the material's mechanical properties.

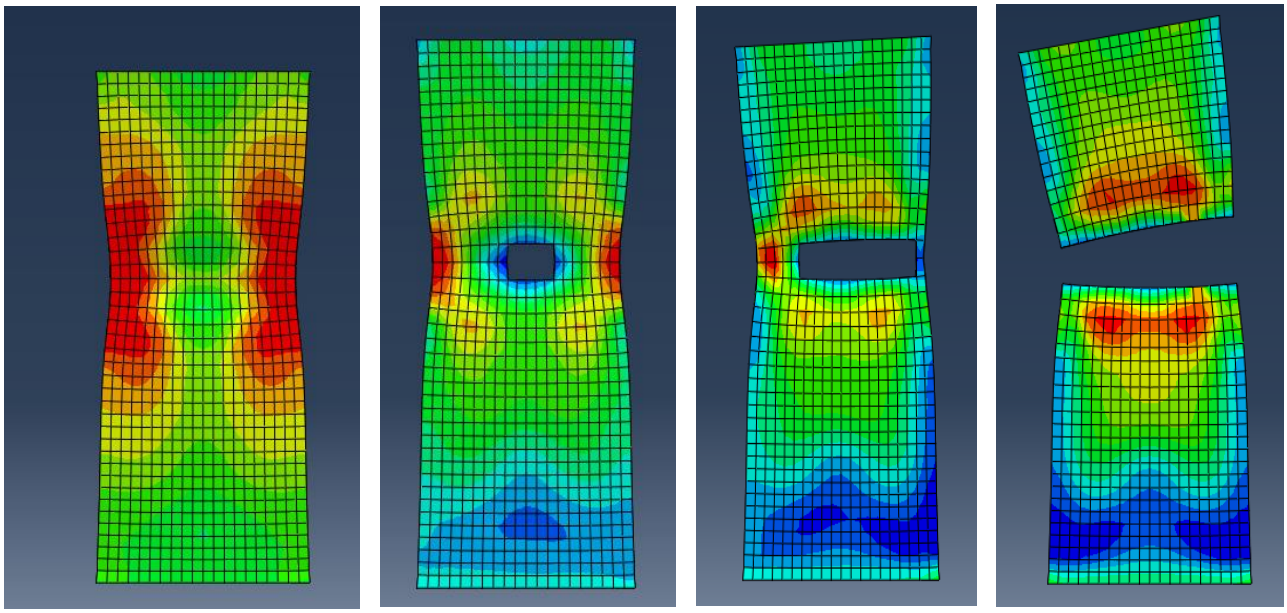

Figure 16 SS316L specimen simulation results

The **von Mises stress distribution** for the SS316L specimen under tensile loading is shown in the simulation images in figure 15. Initially, stress is evenly distributed across the gauge section, but as the deformation progresses, stress concentrations develop near the center of the specimen. The final stage shows localized necking and failure, which aligns well with the observed experimental behavior.

The **force-displacement curve** in figure 16 shows a strong correlation between experimental and FEA data. The initial linear elastic region closely matches, indicating that the elastic modulus was accurately modeled. As the displacement increases, the FEA curve maintains close agreement with experimental data, showing a gradual increase in force until reaching the peak load.

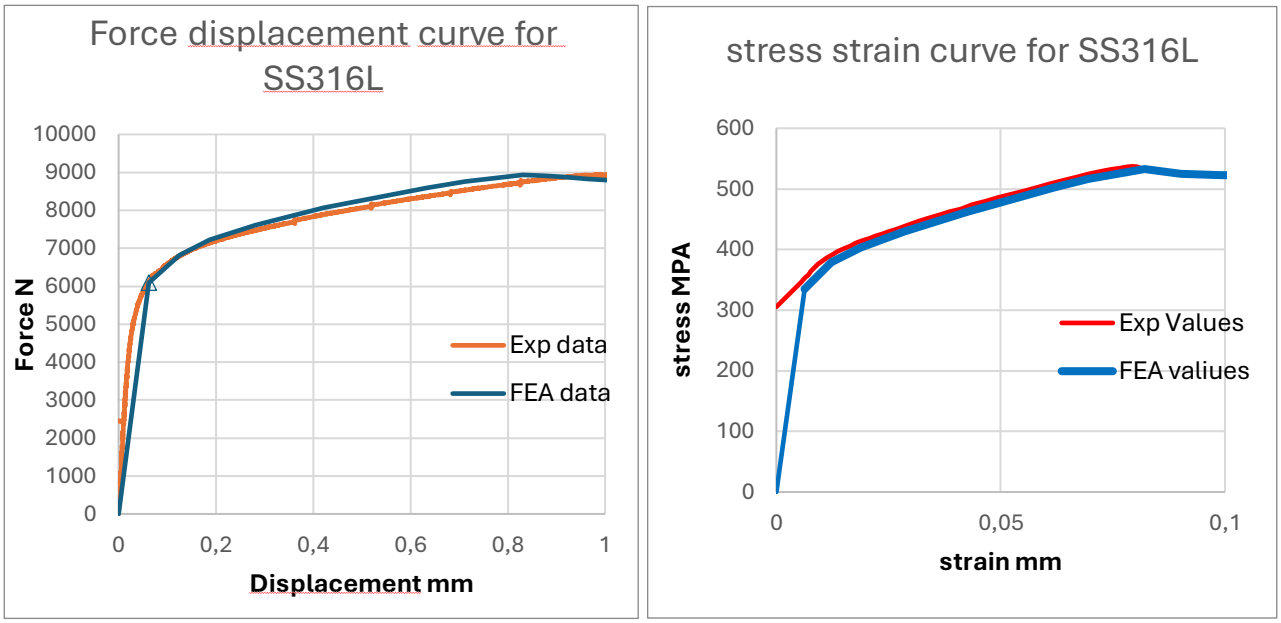

Figure 17 Force displacement curve and stress strain curve of SS316L

The **ultimate tensile strength (UTS)** is captured effectively in the simulation, though minor differences are observed in the softening region due to the limitations in damage evolution modeling.

Similarly, the **stress-strain curve** in figure 16 provides insights into the strain-hardening behavior of SS316L. The **yield stress** is well captured, and the simulation successfully represents the work-hardening phase, where stress increases with strain before reaching a plateau. However, the post-

peak behavior in the FEA model shows a slightly sharper drop compared to the experimental data. This discrepancy may be due to the damage evolution parameters or element deletion criteria applied in the simulation. Adjustments in damage evolution law**,** such as refining the fracture energy or adjusting softening parameters, could improve agreement with experimental results.

In conclusion, the FEA model for SS316L effectively replicates the elastic, plastic, and fracture response of the material under tensile loading. The force-displacement and stress-strain curves indicate strong agreement with experimental data, confirming the validity of the simulation approach. Minor deviations in the post-peak region suggest further refinement of damage and fracture criteria could enhance the accuracy of failure predictions.

4.2.3 Comparison of individual materials:

The comparative analysis of ER70S-6 and SS316L as an individual specimen under tensile loading reveals significant differences in their mechanical behavior, as seen in the force-displacement and stress-strain curves. ER70S-6, a carbon steel used in WAAM applications, exhibits a higher initial yield strength but a relatively lower strain-hardening capacity compared to SS316L, a stainless steel known for its superior ductility. The force-displacement curves for both materials show a close agreement between FEA and experimental results, with ER70S-6 displaying a steeper elastic region and a sudden drop post-ultimate tensile strength, indicating a more brittle fracture behavior. On the other hand, SS316L demonstrates a more gradual transition from yielding to fracture, which aligns with its higher ductility and strain-hardening ability.

The stress-strain curves further highlight these distinctions, where ER70S-6 reaches its ultimate tensile strength (UTS) at a lower strain level compared to SS316L, which continues to sustain stress over a wider strain range. This suggests that SS316L can accommodate higher plastic deformation before failure, making it more suitable for applications requiring enhanced formability and energy absorption. Additionally, the fracture behavior in the FEA simulations indicates that ER70S-6 undergoes localized failure with a sharp drop in stress, while SS316L exhibits a more distributed necking before failure, further confirming its higher ductility. Overall, ER70S-6 provides higher strength but lower ductility, making it suitable for structural applications where rigidity is prioritized. In contrast, SS316L offers a more balanced combination of strength and ductility, making it preferable for applications requiring high toughness and resistance to fracture.

4.3 Multi-material tensile specimen modelling and simulation:

Multi-material tensile specimen without Transition Zone:

As discussed in the methodology, multi-material tensile modeling was carried out using different stacking strategies to evaluate how interface design affects stress distribution and fracture behavior. In this initial trial, a multi-material specimen was created in which ER70S-6 and SS316L were stacked directly—without any gradual transition layer—resulting in a sharp material boundary at the interface. This configuration was purposefully chosen to assess the mechanical consequences of abrupt changes in material properties, particularly the effects on stress concentration and fracture initiation.

The simulation aimed to replicate the behavior of a tensile test specimen in which two dissimilar materials meet at a well-defined, stepwise interface, with no smooth blending of mechanical properties. From a mechanical standpoint, such discontinuity introduces a mismatch in stiffness and plastic behavior, which is expected to manifest as stress concentration at the interface during loading. This design serves as a control case, helping to justify the necessity of introducing a transition zone in later models.

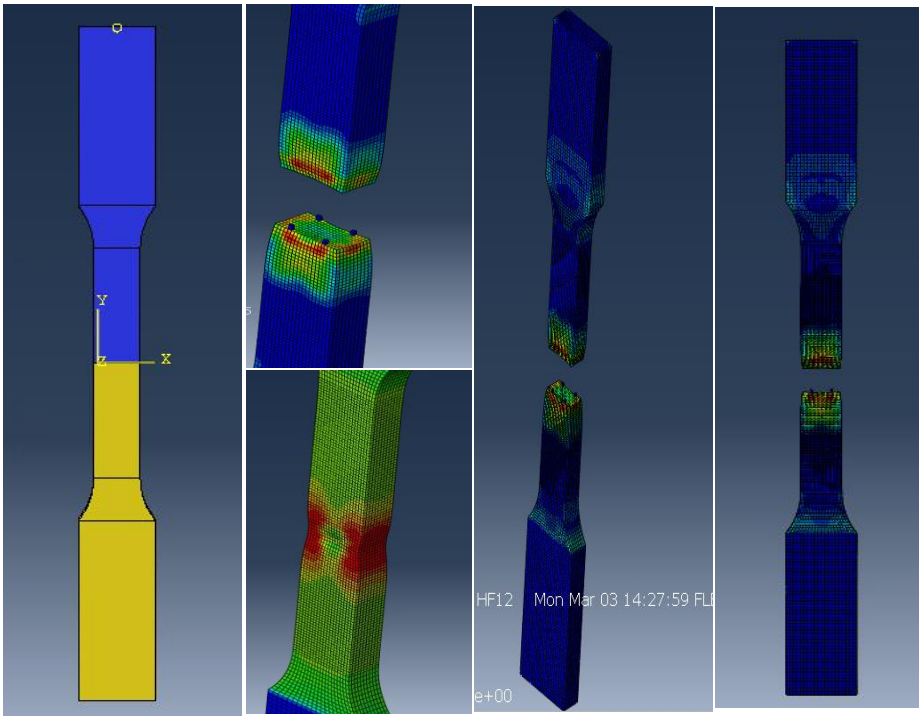

Figure 18 Simulation results of multimaterial specimen without transition zone

As shown in Figure 17, the simulation results clearly demonstrate the development of localized stress concentration exactly at the interface between the two materials. The contour plots of equivalent plastic strain and damage evolution reveal that this region experiences premature failure, even though the surrounding material remains structurally stable. The high-stress gradient is a direct result of discontinuity in Young's modulus and yield strength across the ER70S-6 and SS316L boundary.

Notably, the simulation predicts early crack initiation and propagation starting at the interface, which validates the assumption that stacking two materials without a transition region leads to mechanical instability. This behavior is not just theoretical—it aligns with physical observations in welded and additively manufactured joints, where similar mismatches result in interface-driven failure. The results support the decision to introduce transition layers in subsequent multi-material specimens to allow a gradual transfer of load, reduce stress singularities, and enable better mechanical synergy between dissimilar alloys.

4.4 Multi-material specimens with 9 different material stacking arrangements:

The mechanical response of nine different multi-material specimens, each composed of various stacking arrangements of ER70S-6, SS316L, and transition interface layers, was evaluated under uniaxial tensile loading. These configurations were strategically designed to investigate how the sequence, symmetry, material dominance, and number of transition zones influence the stress distribution, plastic deformation, and fracture behavior of WAAM-fabricated components.

Each specimen featured a unique layout in the gauge region: some with symmetric stacking, others with alternating layers, and a few with mixed sequences that intentionally varied the stress path across the specimen cross-section. The transition zones between materials were included to simulate a realistic WAAM build, where partial fusion or metallurgical blending can occur at interfaces. These layers play a critical role in facilitating gradual stress transfer between dissimilar materials and in suppressing premature interface failure, as observed in the non-transition model.

During the simulations, the same boundary conditions and meshing strategies were applied to all specimens to ensure consistency and comparability. Each model was subjected to displacement-

controlled tensile loading until fracture. Key outputs such as reaction force, strain localization, equivalent stress, and damage evolution were monitored to analyze the mechanical performance.

4.4.1 Specimen 01:

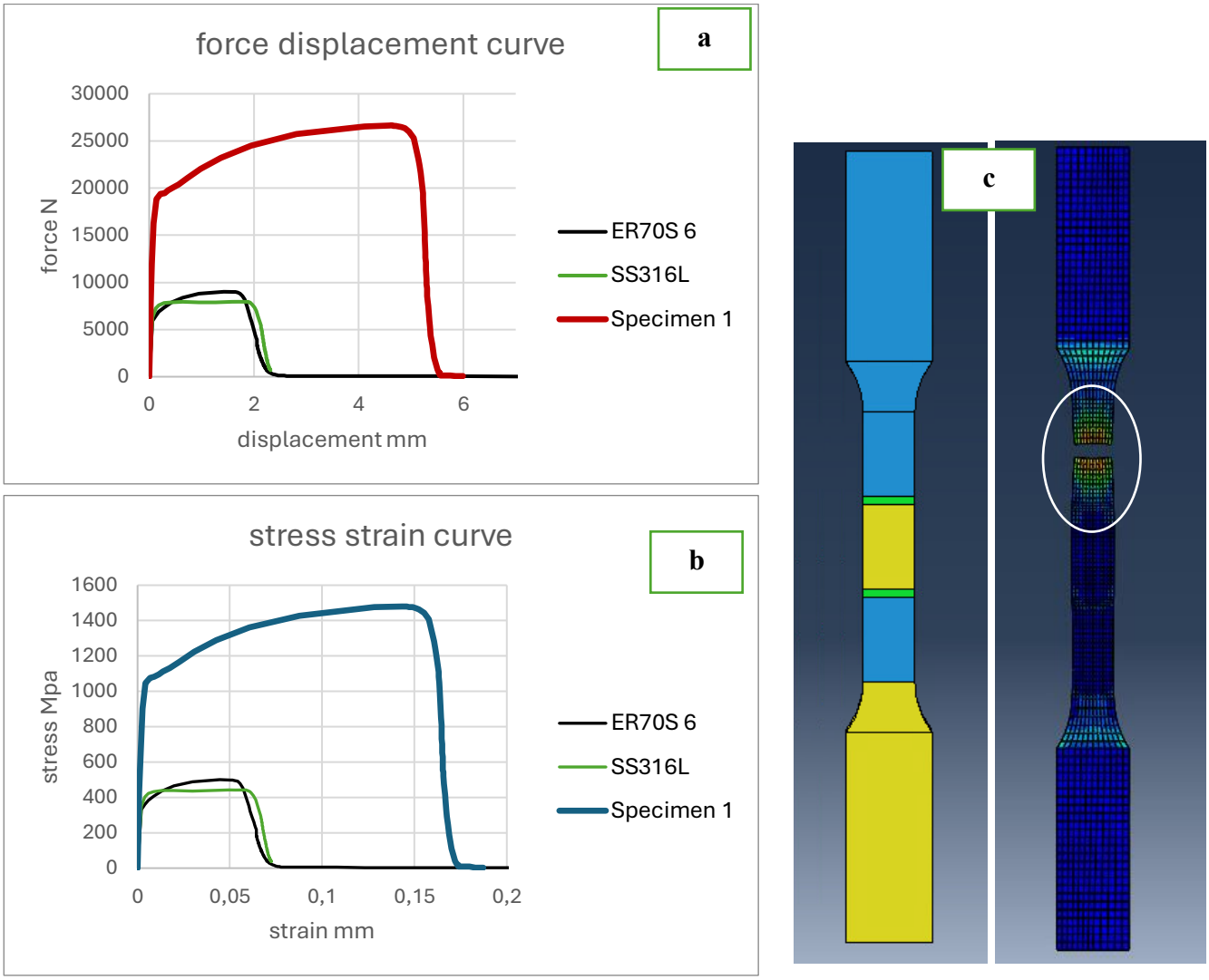

Figure 19 Specimen 1 a) force displacement curve b) stress strain curve c) simulation results

Specimen 1 features a symmetric stacking sequence with ER70S-6 at the outer layers, SS316L at the core, and thin transition zones in between. This configuration was designed to promote gradual stress transfer and balanced mechanical response. The force-displacement curve shows a high initial stiffness and a broad plastic region, reaching a peak load of ~26,800 N at 5.1 mm displacement. The

stress-strain curve reveals a UTS of ~1475 MPa and a fracture strain of ~0.175, indicating excellent strength with moderate ductility.

Compared to both base materials, this specimen shows a 2.5× increase in strength over SS316L and greater ductility than ER70S-6. The transition zones effectively minimize stress concentration, enabling stable load transfer. Fracture initiates near the interface or in the ER70S-6 region after brief necking, suggesting room for further interface optimization. Overall, Specimen 1 demonstrates a well-balanced performance, combining high strength with controlled plastic deformation.

4.4.2 Specimen 2:

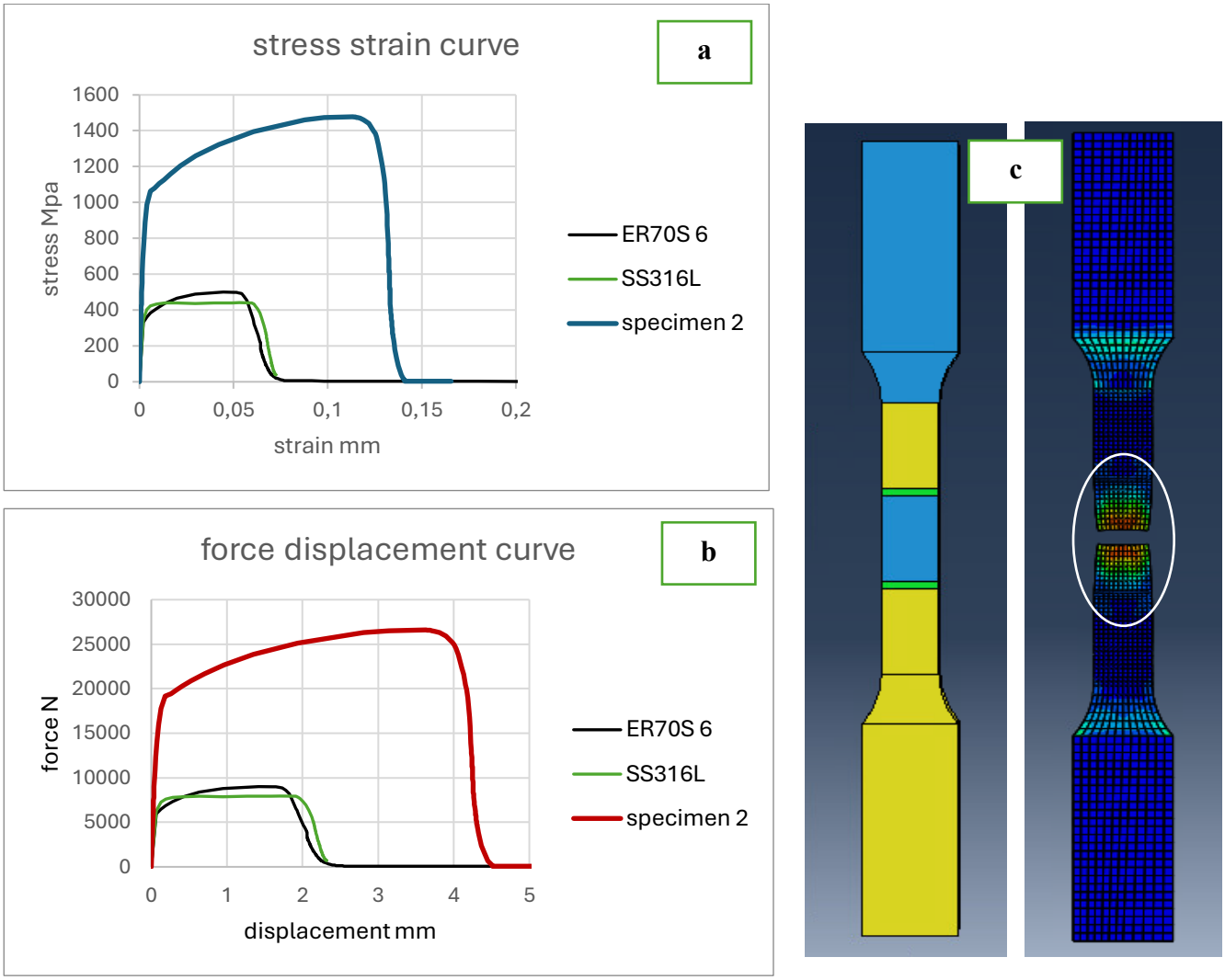

Figure 20 Specimen 2 a) force displacement curve b) stress strain curve c) simulation results

Specimen 2 consists of alternating vertical layers of ER70S-6 and SS316L without clear symmetry. It achieved a UTS of ~1480 MPa and a fracture strain of ~0.145, slightly lower in ductility than Specimen 1. The force-displacement curve shows a steep rise and an earlier drop post-peak, indicating higher stiffness but reduced deformation capacity.

Although stronger than both base materials, the frequent interfaces likely introduced stress mismatches, leading to earlier crack initiation and a more brittle-like fracture. Compared to Specimen 1, the performance trade-off here is clear: strength is retained, but ductility is compromised. This specimen highlights the effect of interface density on limiting strain capacity despite high load resistance.

4.4.3 Specimen 3:

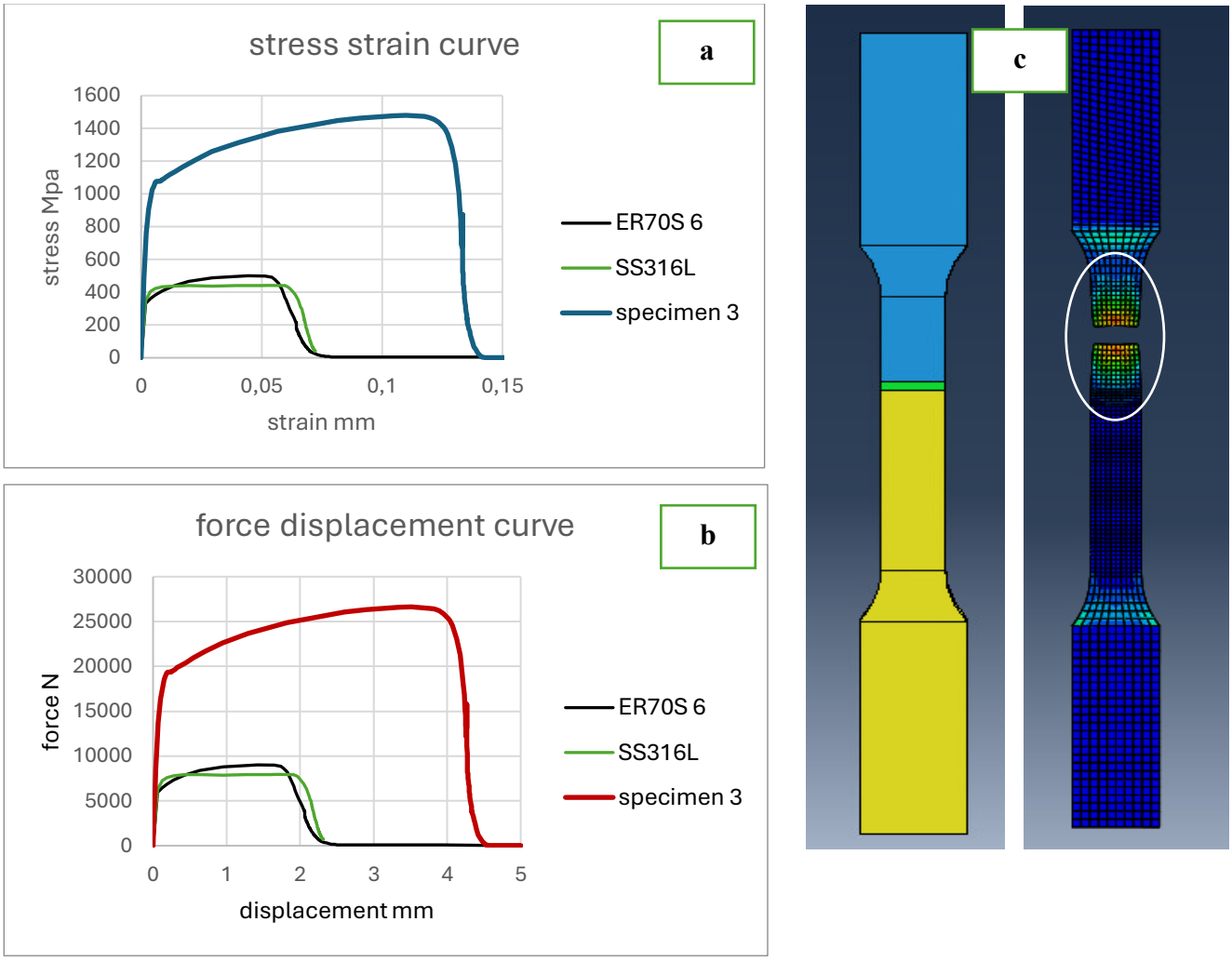

Figure 21 Specimen 3 a) force displacement curve b) stress strain curve c) simulation results

Specimen 3 features an asymmetric stacking configuration, with vertically split regions of ER70S-6 and SS316L and no mirrored symmetry across the gauge section. The specimen reaches a UTS of ~1450 MPa and a fracture strain of ~0.145, comparable in strength to Specimen 2 but with a more abrupt post-peak stress drop. The force-displacement curve indicates early softening after peak load, suggesting that stress was not uniformly distributed. The asymmetric layout likely caused non-uniform strain localization, promoting earlier crack initiation near the interface.

Compared to the base materials, this specimen delivers substantially higher strength and improved ductility but falls short of the smoother performance observed in symmetric designs like Specimen 1. It reinforces that material orientation and stacking symmetry are critical for achieving stable deformation and enhancing fracture resistance in multi-material structures.

4.4.4 specimen 4:

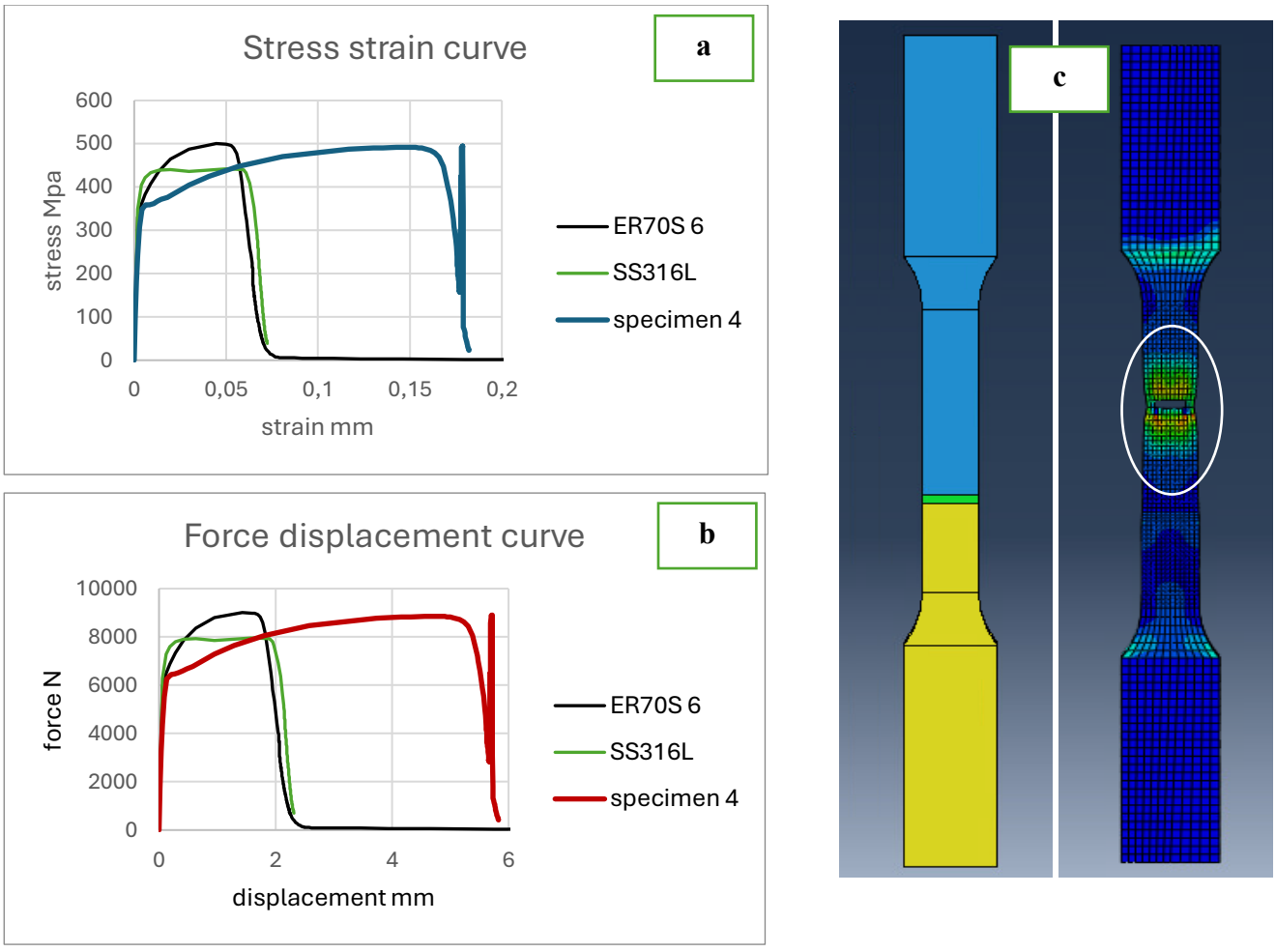

Figure 22 Specimen 4 a) force displacement curve b) stress strain curve c) simulation results

Specimen 4 features a vertically stacked configuration, with ER70S-6 as the dominant material occupying the majority of the gauge length, and SS316L at the bottom, separated by a thin transition zone. While the material sequence mirrors that of Specimen 3 (ER70S-6 on top, SS316L below), the two differ significantly in mechanical response due to the inverted material dominance. This specimen records a UTS of only ~500 MPa, which is substantially lower than Specimen 3 (~1450 MPa), and maintains a fracture strain of ~0.18, indicating a more ductile but weaker behavior.

The force-displacement curve of Specimen 4 shows a broad, nearly plateau-like plastic region followed by a delayed but sudden failure. Meanwhile, the stress-strain curve displays a gradual hardening response with no sharp peak, followed by a soft and unstable drop. This indicates that the dominance of the softer ER70S-6 material governs deformation, allowing the specimen to stretch significantly but failing to carry high tensile loads. Despite the presence of a transition zone, the high proportion of ER70S-6 reduces the overall stiffness and strength of the specimen.

Additionally, the unnatural flatness observed in the post-yield region may arise from progressive damage accumulation in ER70S-6, which fails slowly and spreads across the gauge section. This behavior aligns with ductile tearing rather than abrupt fracture, particularly as the harder SS316L at the base does not control the fracture path. The transition zone remains intact longer, and failure is not interface-driven but rather dictated by bulk yielding of the ER70S-6 region.

In conclusion, Specimen 4 illustrates how the position and volume of each material within the stacking sequence drastically influences tensile behavior. Even with a transition zone, placing ER70S-6 as the dominant stress-bearing material limits the peak strength while promoting elongation. The resulting behavior is ductile, energy-absorbing, but structurally weak, making this configuration less suitable for high-strength applications but potentially useful where flexibility is critical.

4.4.5 Specimen 5:

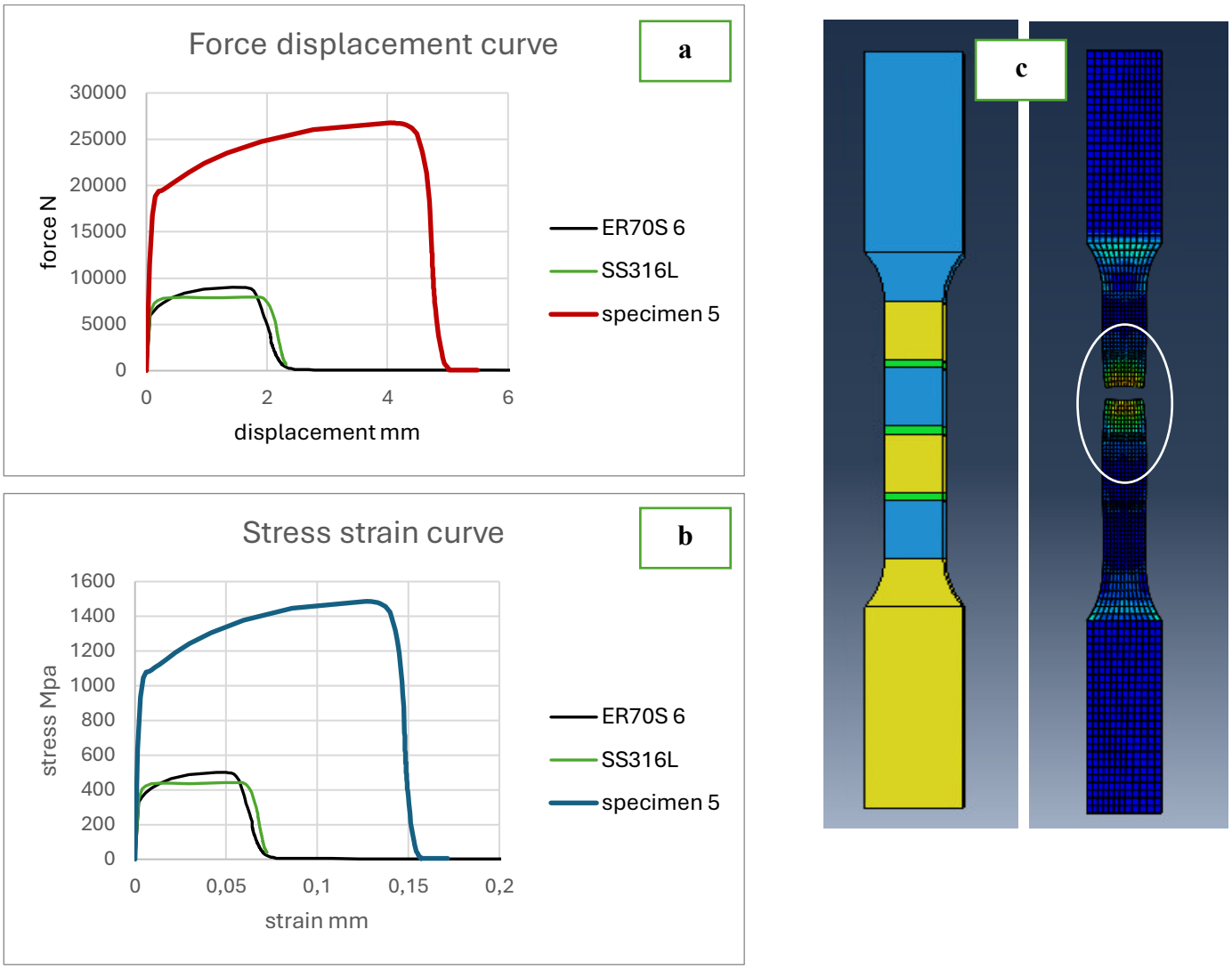

Figure 23 Specimen 5 a) force displacement curve b) stress strain curve c) simulation results

Specimen 5 consists of alternating vertical layers of ER70S-6 and SS316L with a more balanced and gradual transition than Specimen 2. It achieves a UTS of ~1475 MPa and a fracture strain of ~0.155, placing it just below Specimens 1 and 6 in ductility. The force-displacement response shows a high peak load with a smoother post-UTS decline than other alternating configurations, indicating improved stress continuity.

It significantly outperforms both base materials in strength and elongation. The more controlled layering appears to reduce interface-induced stress concentrations, resulting in a strong and

moderately ductile configuration. This specimen demonstrates that alternating stacks can perform well if transitions are gradual and layer thickness is well balanced.

4.4.6 Specimen 6:

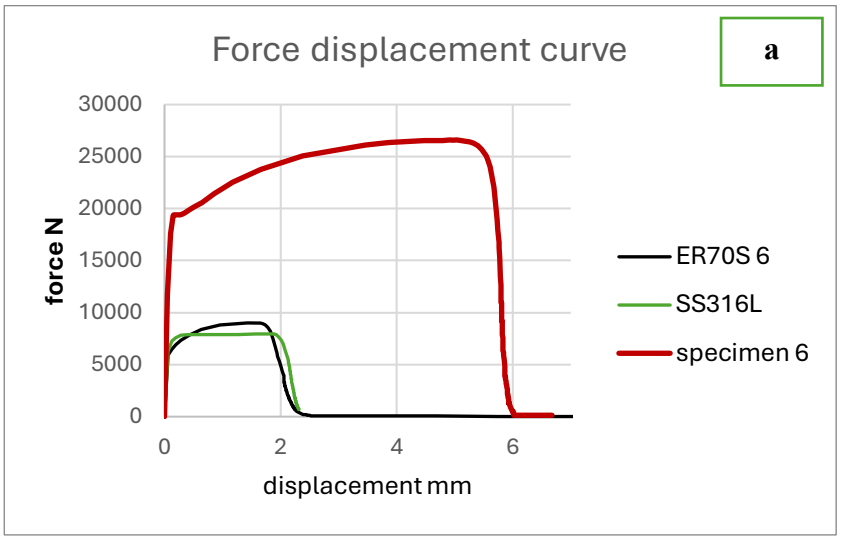

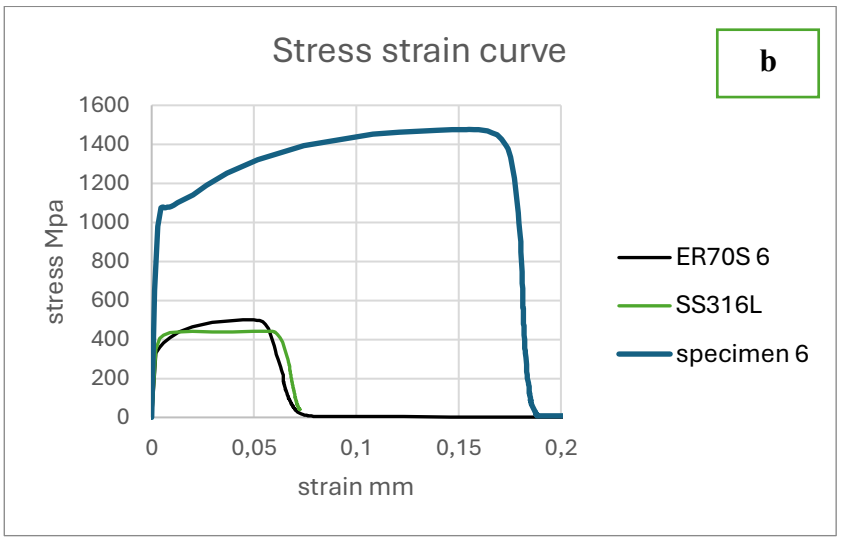

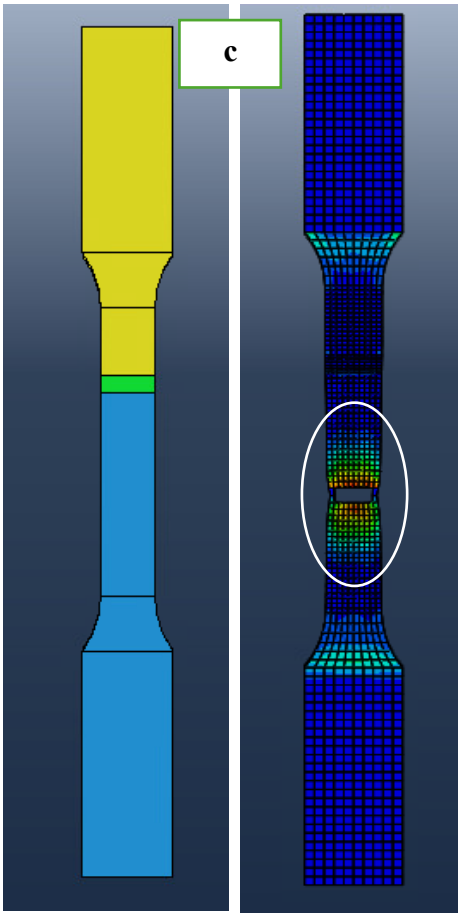

Figure 24 Specimen 6 a) force displacement curve b) stress strain curve c) simulation results

Specimen 6 incorporates a symmetric, ER70S-6-dominant stack, with SS316L layers placed near the interfaces and thin transition zones between materials. This configuration delivers the best overall performance, with a UTS of ~1480 MPa and the highest fracture strain among high-strength specimens (~0.195). The stress-strain curve shows a long strain-hardening region and a stable post-peak decline, indicating excellent energy absorption and delayed failure.

Compared to both base materials, Specimen 6 exhibits over 2.5× the strength of SS316L and superior ductility. Its symmetrical design ensures uniform stress flow and minimizes localization. The effective use of transition zones contributes to smooth load redistribution, making this specimen a model example of optimal multi-material design for structural performance.

4.4.7 Specimen 7:

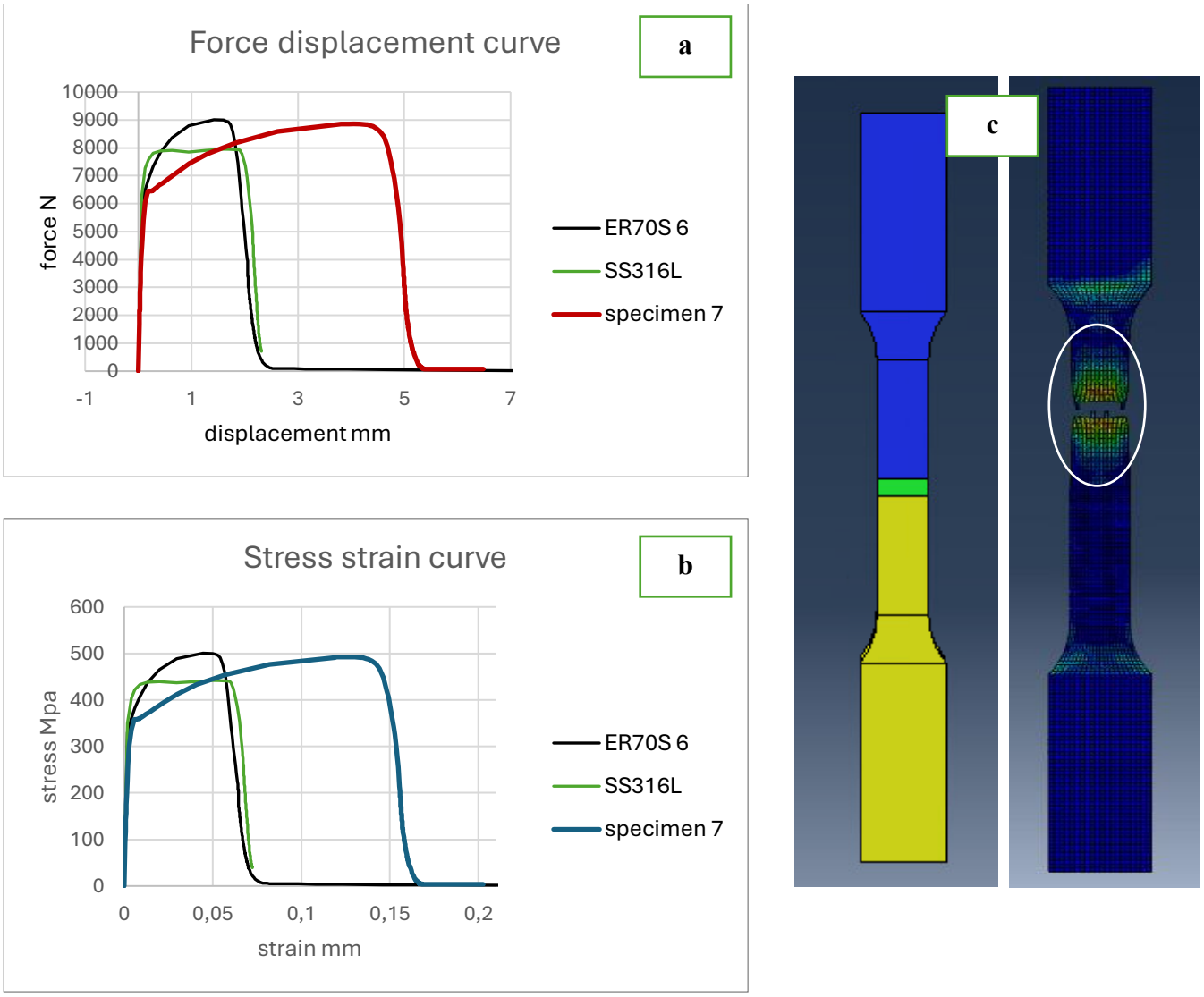

Figure 25 Specimen 7 a) force displacement curve b) stress strain curve c) simulation results

Although Specimen 7 uses the same number of layers and a symmetric stacking layout as Specimen 6, it differs in material distribution, with SS316L dominating the core and ER70S-6 positioned at the outer surfaces. As a result, it exhibits a much lower UTS (~500 MPa) but maintains a high

fracture strain (~0.18). The force-displacement curve shows a long plastic region and a gradual decline, indicating excellent ductility but limited strength.

Compared to the base SS316L, the specimen behaves similarly in strength and surpasses it in elongation. This contrast with Specimen 6 demonstrates that material dominance in the stress-bearing region critically affects performance. While symmetric in geometry, the reduced strength highlights that stacking layout alone is not sufficient—material positioning must also be optimized for desired outcomes.

4.4.8 Specimen 8:

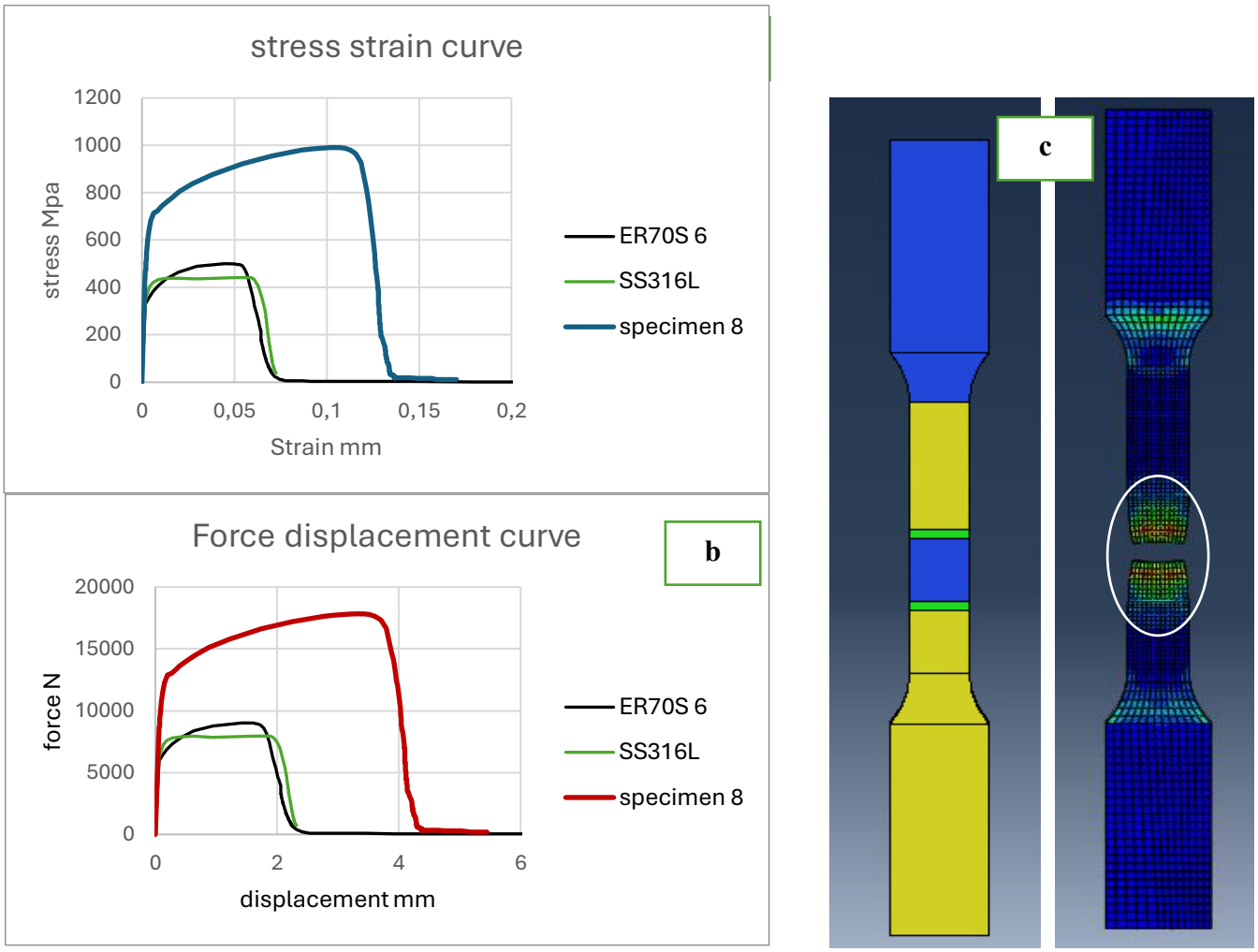

Figure 26 Specimen 8 a) force displacement curve b) stress strain curve c) simulation results

Specimen 8 adopts a sandwich-style configuration, placing a ductile SS316L core between outer layers of ER70S-6, aiming to blend high strength with elongation. It reaches a UTS of ~1000 MPa

and achieves the highest fracture strain (~0.41) among all specimens. The stress-strain curve features a long, smooth hardening phase and a stable post-peak drop, indicating high energy absorption and excellent deformation capacity.

This specimen far exceeds both base materials in ductility and significantly improves strength compared to SS316L. Stacking effectively leverages the strength of ER70S-6 while relying on the ductility of SS316L to control crack propagation. Specimen 8 is ideally suited for flexibility-dominant applications, proving how hybrid stacking can be tailored to meet high-strain requirements without sacrificing strength completely.

4.4.9 specimen 9

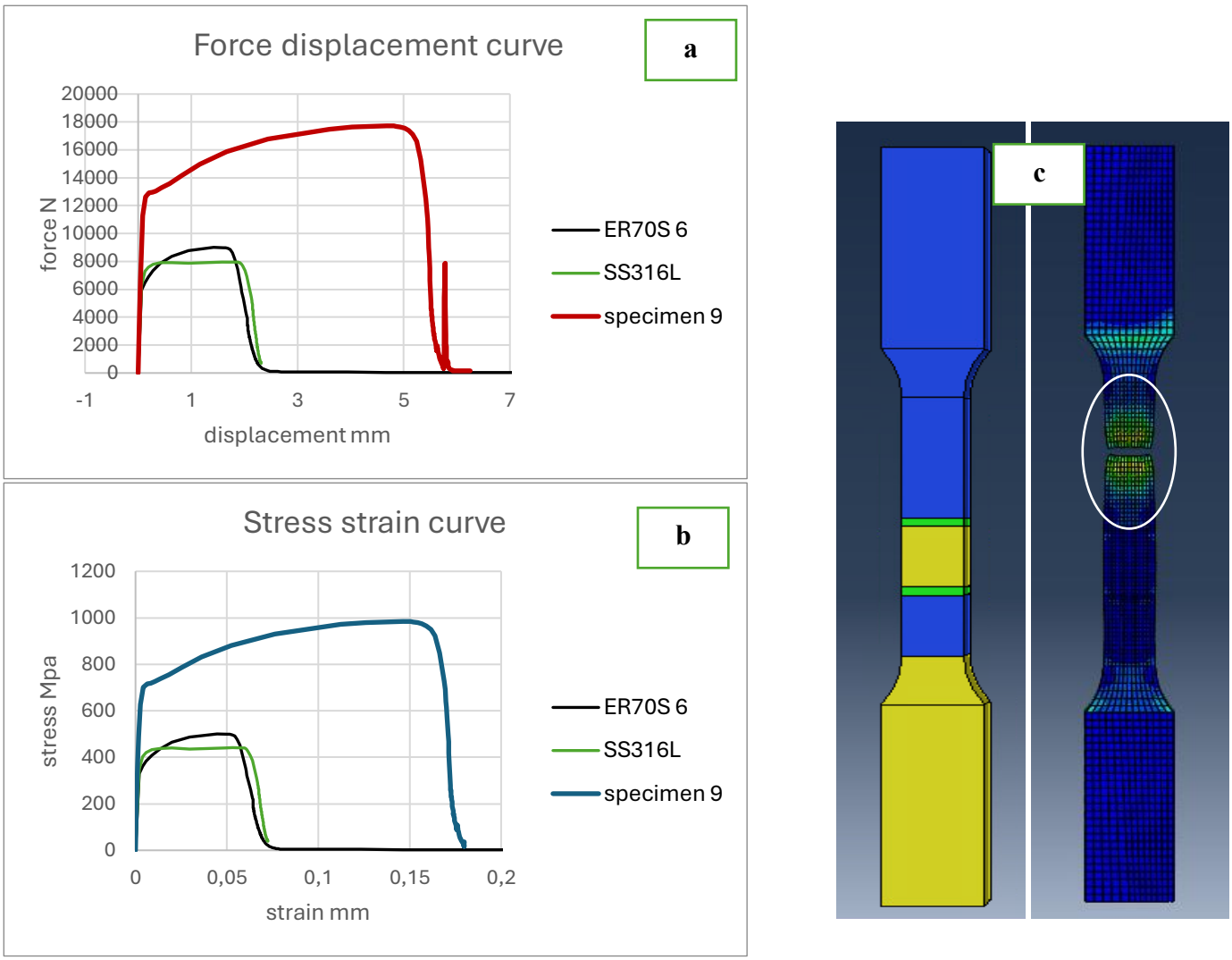

Figure 27 Specimen 9 a) force displacement curve b) stress strain curve c) simulation results

Specimen 9 is designed with a multi-layered stacking configuration, where alternating blocks of ER70S-6 and SS316L are arranged symmetrically along the gauge length, separated by multiple transition zones. This layout aims to evenly distribute mechanical properties along the tensile axis, but introduces a high density of interfaces, which significantly affects the fracture mechanism. The specimen reaches a UTS of ~1000 MPa, and a fracture strain of ~0.16, indicating moderate strength and good ductility. However, the post-UTS behavior is notably abnormal, as seen in both the force-displacement and stress-strain curves, which display a brief force resurgence or rebound after initial load drop.

This behavior suggests the occurrence of multi-stage failure. As damage initiates and local fracture begins near one interface, other material segments continue to carry load, causing non-uniform stress redistribution across adjacent layers. This may momentarily stabilize the structure or shift the load path to another segment, resulting in the observed "bump" or fluctuation in the force curve. The simulation results confirm this, showing stress concentration spread across multiple interfaces instead of a single dominant failure zone.

Although the configuration delivers a better ductility-to-strength balance than the individual base materials, the abundance of transitions likely delays but complicates the fracture process. The curve does not show a clean drop post-UTS, as seen in Specimens 1–6, but instead reflects unstable crack progression and delayed element deletion in Abaqus due to the layered design.

Table 3 Tensile properties of all 9 specimens

specimens	Young modulus (Mpa)	yield stress (f_γ or σ_γ))	Epsilon at Yield (ε_γ or ε_yield)	Ultimate Tensile stress (UTS, Fu)	Epsilon at Ultimate (ε_u or ε_UT)	Strain-hardening capacity (F_u / F_γ)	Ductility (ε_u / ε_γ)	fracture stress	fracture strain
1	9300	1100	0.002	1475	0.155	1.34	77.5	1300	0.175
2	8700	1100	0.002	1480	0.125	1.34	62.5	1300	0.145

3	8500	1080	0.002	1450	0.125	1.34	62.5	1250	0.145
4	4000	360	0.002	500	0.16	1.39	80	450	0.18
5	8600	1100	0.002	1475	0.14	1.34	70	1350	0.155
6	9000	1120	0.002	1480	0.175	1.32	87.5	1400	0.195
7	3800	350	0.002	500	0.16	1.43	80	450	0.18
8	7000	680	0.002	1000	0.12	1.47	60	850	0.155
9	7200	700	0.002	1000	0.155	1.43	77.5	850	0.18

4.5 Comparison of force displacement curves of all 9 specimens:

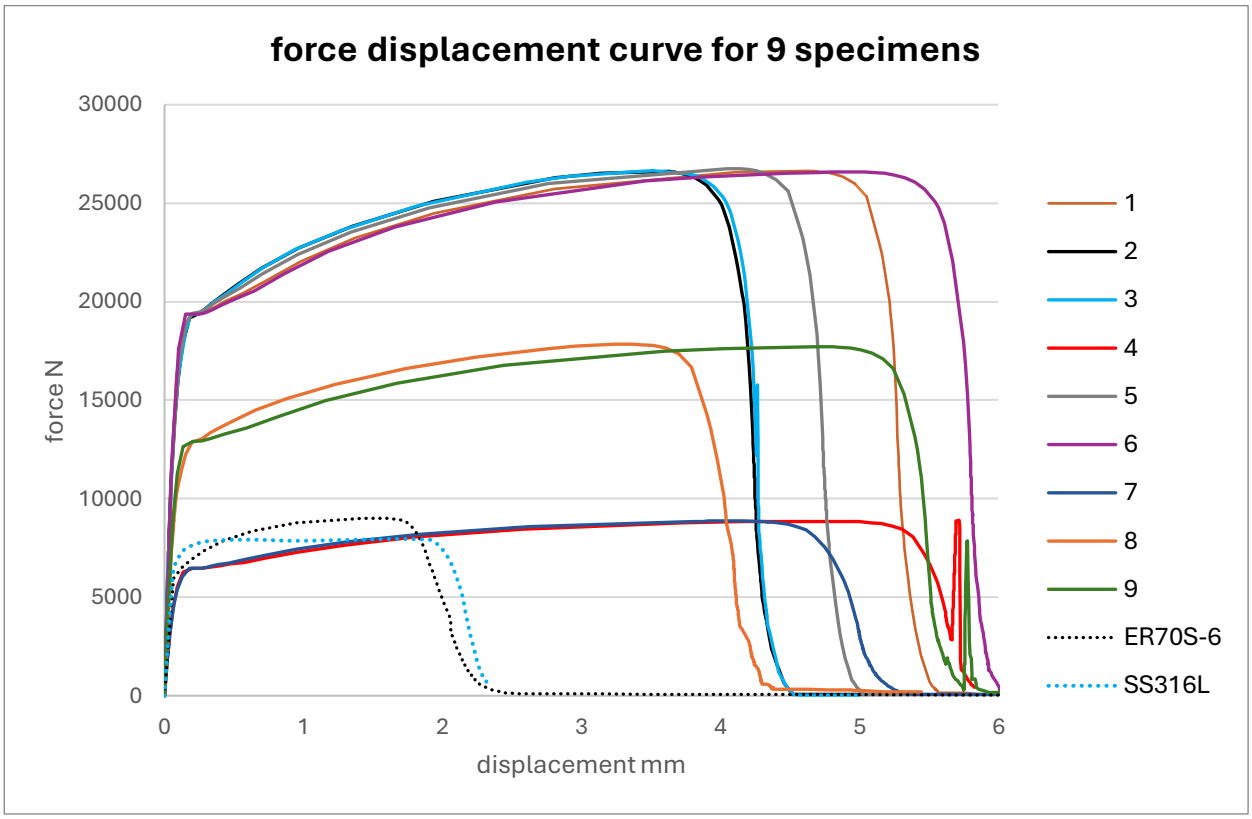

Figure 28 Comparison of force displacement curves of all 9 specimens and base materials

The force-displacement curves of the nine WAAM-fabricated multi-material tensile specimens exhibit three distinct mechanical response groups, shaped by stacking arrangement, material dominance, and transition zone placement. Despite using the same base materials—ER70S-6 and SS316L—each specimen's behavior is uniquely governed by how these materials are distributed and interact during loading.

Specimens 1, 2, 3, 5, and 6 form the high-strength group, each achieving peak forces above 26,000 N. Among them, Specimen 6 demonstrates the best mechanical performance, with the highest load (~26,900 N) and the longest displacement (~6 mm). Its symmetric ER70S-6-dominant stacking with well-placed transition zones ensures smooth load transfer, broad plasticity, and delayed failure. Specimen 1 follows closely, offering balanced strength and ductility with minimal post-peak instability—evidence of effective stress sharing across the gauge section.

Specimen 2 matches the strength of the top performers but exhibits a sharper post-UTS drop, likely due to stress accumulation at frequent vertical interfaces. Specimen 3, though structurally similar to Specimen 4, benefits from SS316L dominance and achieves a high peak force (~1450 MPa) but with earlier failure, reflecting limited ductility. Specimen 5, featuring alternating layers with controlled transitions, delivers stable force buildup but slightly reduced elongation—its earlier post-peak drop suggests stress localization from microcrack accumulation across multiple interfaces.

In contrast, Specimens 4, 7, 8, and 9 show lower peak forces (ranging from ~8,900 N to ~18,000 N) but relatively higher displacements, prioritizing ductility and energy absorption. Specimen 8 stands out among them, exhibiting the smoothest post-peak behavior and the highest fracture strain (~0.41). Its layered structure effectively blends ductility and strength, allowing stable yielding throughout the gauge length. Specimen 7 also features prolonged displacement and good flexibility, though its load capacity remains limited. Specimen 4, despite having the same stacking as Specimen 3, underperforms due to ER70S-6 dominance. The weaker material governs the tensile response, limiting strength but supporting elongation—its post-peak instability reflects a sudden failure following necking.

Specimen 9 displays unique fluctuations in the post-UTS region, suggesting unstable crack propagation across its multiple transitions. Although its strength and ductility are moderate, the force rebound indicates complex multi-site failure behavior, reducing predictability and making it less suitable for critical applications.

Despite their differences, the specimens reveal important design trends. Symmetric stacking with appropriate transitions (e.g., Specimen 6) leads to enhanced energy absorption and stable failure. Dominant placement of the stronger material within the stress path (as in Specimen 3) increases peak force, while excess interfaces (as in Specimen 9) compromise fracture stability. These insights emphasize that performance is not simply defined by material type but by how those materials are architecturally integrated.

In summary, Specimen 6 is ranked highest for its overall mechanical efficiency, followed by Specimens 1 and 5 for their strong and balanced responses. Specimen 8 leads in ductility but with lower strength, while Specimen 9, though moderate in performance, suffers from instability. Specimen 4 ranks lowest due to its reduced strength and sudden fracture, despite good elongation. These comparisons underscore the critical role of multi-material design in tailoring tensile behavior through WAAM stacking strategies.

4.6 Comparison of stress strain curves for 9 specimens:

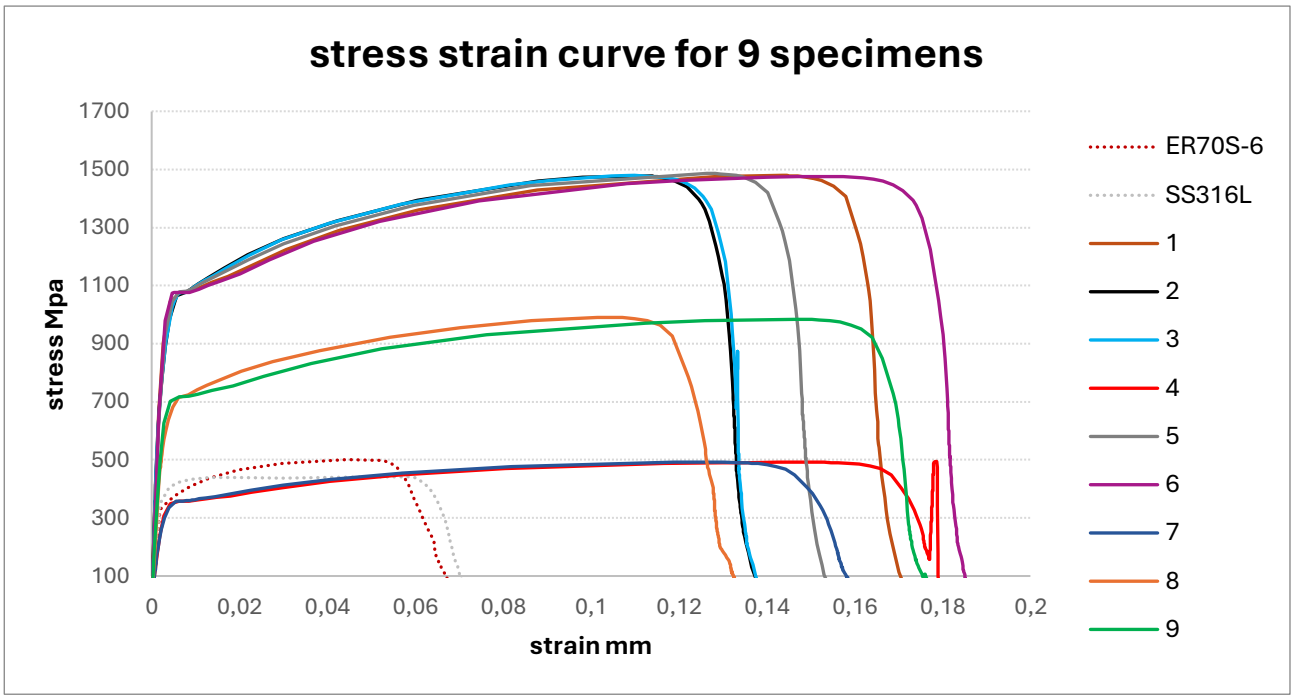

Figure 29 Comparison of stress strain curves for 9 specimens and base materials

The stress-strain curves of the nine WAAM-fabricated multi-material tensile specimens show clear divergence in mechanical behavior, shaped by stacking arrangement, material dominance, and transition zone placement. While all specimens use ER70S-6 and SS316L, their strength, ductility, and post-UTS response vary significantly based on how the materials are distributed within the gauge section.

Specimens 1, 2, 3, 5, and 6 form the high-strength group, with ultimate tensile strengths (UTS) exceeding 1450 MPa. Among them, Specimen 6 offers the best overall performance, achieving the highest ductility (~0.195 strain) and a smooth post-UTS decline. Its symmetric, ER70S-6-dominant layout with effective transition zones supports stable strain hardening and delayed fracture. Specimen 1 follows closely with comparable strength and slightly lower strain (~0.175), offering good balance between load-bearing and elongation.

Specimen 2, though strong (~1480 MPa UTS), shows a more abrupt post-peak drop and lower ductility (~0.145), likely due to stress localization at its frequent vertical interfaces. Specimen 3,

with similar strength but lower strain (~0.135), demonstrates that SS316L dominance contributes to earlier failure despite strong initial performance. Specimen 5 also reaches high strength (~1475 MPa) and moderate ductility (~0.155), but its multiple transitions appear to concentrate stress, triggering faster post-UTS decline.

In contrast, Specimens 4, 7, 8, and 9 prioritize ductility over peak stress. Specimen 8 stands out with the highest fracture strain (~0.41), a long plastic region, and a smooth post-UTS decline, making it ideal for energy-absorbing applications. Specimen 7, though low in strength (~500 MPa), shows good ductility (~0.38 strain) and a flat, stable curve, reflecting excellent deformation tolerance.

Specimen 4, despite matching the stacking of Specimen 3, shows a UTS of only ~500 MPa due to ER70S-6 dominance, though it maintains a stable yielding phase and fracture strain of ~0.18. Specimen 9, with moderate UTS (~1000 MPa) and strain (~0.34), displays erratic post-peak behavior, likely due to its many interfaces causing multi-site crack propagation and unstable stress redistribution.

These results highlight key design insights: symmetric stacking and strong transition zones (Specimens 1 and 6) enhance both strength and ductility. Material dominance directly affects performance—SS316L improves UTS (Specimen 3), while ER70S-6 improves ductility (Specimen 4). Meanwhile, excessive layering (Specimen 9) compromises fracture stability.

In summary, Specimen 6 ranks highest for combined strength and ductility, followed by Specimens 1 and 5 for their balanced performance. Specimen 8 is the most ductile, while Specimen 9 offers moderate values but unstable fracture. Specimen 4, though stable, ranks lowest in strength. Together, these findings reinforce the role of stacking architecture in controlling mechanical behavior of WAAM-fabricated multi-material specimens.

Table 4 Summarize properties of 3 groups of curves

Group	Specimens	Performace highlights	Fracture behavior
Group 1: High Strength + Moderate Ductility	1, 2, 3, 5, 6	UTS > 1450 MPa; best performer: Specimen 6 with smooth load transfer and broad plastic zone. Specimens 2 and 3 showed earlier failure due to abrupt transitions.	Fracture occurred after moderate strain; strong but slightly brittle in specimens with asymmetric layouts.
Group 2: Moderate Strength + High Ductility	8, 9	UTS ~1000 MPa; high fracture strain (~0.34–0.41); Specimen 8 had highest strain at failure with stable plastic deformation.	Gradual and stable fracture; capable of dissipating stress evenly despite moderate strength.
Group 3: Low Strength + Maximum Ductility	4, 7	UTS ~500 MPa; maximum elongation and energy absorption. Suitable for applications demanding high toughness rather than strength.	Very stable fracture with wide plastic zones; necking and failure occurred smoothly without stress spikes.

5 Conclusions:

This thesis presented a comprehensive computational investigation of the mechanical behavior of multi-material components fabricated by Wire Arc Additive Manufacturing (WAAM), focusing on tensile performance under varying stacking configurations of ER70S-6 and SS316L. Using Abaqus-based finite element simulations, nine unique multi-material tensile specimens were designed to explore the effects of material arrangement, interface positioning, and transition zone design on key mechanical properties such as ultimate tensile strength, ductility, strain-hardening behavior, and fracture stability.

Despite using only two base materials, the simulation results revealed that internal stacking architecture dramatically alters mechanical response. Three distinct behavioral groups were identified: high-strength (Specimens 1, 2, 3, 5, 6), high-ductility with moderate strength (Specimens 8 and 9), and low-strength with maximum elongation (Specimens 4 and 7). These groupings were governed by how material dominance, stacking symmetry, and interface continuity influenced stress flow and failure modes.

Among all configurations, Specimen 6 emerged as the most mechanically efficient design, combining the highest UTS (~1480 MPa) with excellent ductility (~0.195 strain). Its symmetric ER70S-6-dominant layout and well-placed transition zones provided smooth load transfer, broad plastic deformation, and stable post-yield behavior. Specimen 1 followed closely, offering slightly lower ductility but similar strength, while Specimen 5 demonstrated consistent strength with moderate strain-hardening—though earlier post-UTS decline hinted at stress localization due to multiple interfaces. Specimens 2 and 3, despite achieving high UTS, fractured earlier due to their interface-rich or asymmetric designs, leading to reduced elongation and more abrupt post-peak behavior.

On the opposite end of the spectrum, Specimens 8 and 9 prioritized ductility over strength, with fracture strains above 0.34. Specimen 8, in particular, achieved the highest ductility (~0.41) while maintaining a smooth yielding profile. However, Specimen 9 exhibited post-UTS instability due to its complex layered architecture, where stress redistribution across closely spaced interfaces led to fluctuating fracture progression.

Specimens 4 and 7, both governed by ER70S-6 dominance, recorded the lowest UTS (~500 MPa) but demonstrated consistent and gradual strain hardening up to failure. These configurations highlight the trade-off between load-bearing capacity and energy absorption—emphasizing that stacking decisions can be tailored to application-specific mechanical demands.

A critical observation was that stacking symmetry and number of interfaces alone did not determine performance. For instance, although Specimens 6 and 7 shared a similar symmetric structure and transition layout, their tensile responses diverged significantly due to material dominance. This reinforces the conclusion that interface placement within the gauge region and the directional role of each material in load transfer are key to tuning performance.

Compared to base materials, all hybrid specimens offered significant improvements—up to 3× higher tensile strength and over 5× greater ductility. The addition of transition zones proved essential, consistently reducing stress concentrations and preventing premature interface failure. Most fractures initiated near the interface, reaffirming the need for careful transition design in WAAM-fabricated parts.

Finally, the simulation framework developed on CSC Puhti enabled high-fidelity modeling of complex geometries, validated against available experimental data. The approach proved effective in predicting both global mechanical behavior and local fracture phenomena without relying solely on costly multi-material testing.

In conclusion, this work confirms that multi-material design in WAAM can be strategically leveraged to tailor tensile behavior by manipulating material distribution alone. The study provides practical guidelines for optimizing strength, ductility, or a desired balance through stacking strategies, offering valuable insight for the development of next-generation components with spatially engineered properties—without changing the base materials.

6 Future work and recommendations:

While the finite element simulations conducted in this study provided detailed insights into the tensile behavior of WAAM-fabricated multi-material specimens, future research should extend into experimental validation. Physical fabrication and tensile testing of the nine stacking configurations will be crucial for confirming the computational findings. This includes characterizing the actual fracture locations, load-displacement response, and failure mechanisms, especially in and around the transition zones. Additionally, the microstructural characteristics of the interfaces—such as bonding quality, grain continuity, and local hardness—should be analyzed through methods like SEM, EDS, or EBSD to bridge the gap between computational assumptions and real-world material behavior.

The current simulations assume ideal bonding conditions between materials and exclude the influence of thermal effects. In reality, the WAAM process introduces thermal gradients and residual stresses, which can significantly impact mechanical behavior, especially at material interfaces. Future studies should incorporate coupled thermal-mechanical simulations to capture heat input, cooling rates, and the resulting residual stress fields. This would allow for more accurate predictions of distortion, warping, or early failure due to thermal mismatch—factors that are especially critical when dissimilar materials are used.

To further explore fracture mechanisms, advanced modeling technique's such as the Extended Finite Element Method or Cohesive Zone Modeling should be employed. These methods can simulate crack initiation, propagation, and potential delamination across transition interfaces under both monotonic and cyclic loading. Such approaches would enhance understanding of interfacial fracture toughness and provide insight into local damage evolution—something not fully captured by the current ductile damage models.

Considering that WAAM components are often subjected to cyclic or dynamic loads in service, it is important that future work investigates the fatigue performance of these multi-material specimens. Understanding how stacking arrangement, transition design, and material dominance affect crack initiation and growth under repeated loading will be key to ensuring long-term durability of such structures.

Moreover, future research should aim to develop micromechanical models that account for heterogeneous interfacial behavior. Material models that reflect actual interfacial gradients in strength, stiffness, or ductility would improve prediction fidelity, especially under complex loading scenarios. This could be achieved through localized nanoindentation and microstructure-informed simulations.

To enhance design efficiency, integration of optimization tools—such as genetic algorithms or machine learning—should be explored to identify optimal stacking sequences, transition thicknesses, and material distributions for targeted performance metrics. Automated optimization frameworks could significantly accelerate the design of high-performance multi-material structures.

Finally, the scope of mechanical testing should be expanded beyond uniaxial tension to include shear, biaxial, and impact loading conditions. Real-world components often experience multi-axial stress states or sudden load events such as crash, blast, or pressure cycling. Studying the performance of multi-material WAAM components under such conditions would provide a more holistic understanding of their structural integrity and practical applicability.

7 References:

[1] L. P. Raut and R. V. Taiwade, “Microstructure and Mechanical Properties of Wire Arc Additively Manufactured Bimetallic Structure of Austenitic Stainless Steel and Low Carbon Steel,” *J. Mater. Eng. Perform.*, vol. 31, no. 10, pp. 8531–8541, Oct. 2022, doi: 10.1007/s11665-022-06856-8.

[2] T. DebRoy *et al.*, “Additive manufacturing of metallic components – Process, structure and properties,” *Prog. Mater. Sci.*, vol. 92, pp. 112–224, Mar. 2018, doi: 10.1016/j.pmatsci.2017.10.001.

[3] A. Queguineur *et al.*, “Digital design and manufacturing of a railway bogie demonstrator via multi-material wire arc directed energy deposition,” *Int. J. Adv. Manuf. Technol.*, Feb. 2025, doi: 10.1007/s00170-025-15132-7.

[4] A. Bandyopadhyay and B. Heer, “Additive manufacturing of multi-material structures,” *Mater. Sci. Eng. R Rep.*, vol. 129, pp. 1–16, Jul. 2018, doi: 10.1016/j.mser.2018.04.001.

[5] T. S. Senthil, S. Ramesh Babu, M. Puviyarasan, and V. Dhinakaran, “Mechanical and microstructural characterization of functionally graded Inconel 825 - SS316L fabricated using wire arc additive manufacturing,” *J. Mater. Res. Technol.*, vol. 15, pp. 661–669, Nov. 2021, doi: 10.1016/j.jmrt.2021.08.060.

[6] A. Yadav, M. Srivastava, P. K. Jain, and S. Rathee, “Microstructure and tribological behaviour of dissimilar steel functional structure developed via arc-based DED process,” *Tribol. Int.*, vol. 197, p. 109782, Sep. 2024, doi: 10.1016/j.triboint.2024.109782.

[7] J. Ding, P. Colegrove, J. Mehnen, S. Williams, F. Wang, and P. Almeida, “A computationally efficient finite element model of wire and arc additive manufacture,” *Int. J. Adv. Manuf. Technol.*, vol. 70, pp. 227–236, Jan. 2014, doi: 10.1007/s00170-013-5261-x.

[8] E. R. Denlinger and P. Michaleris, “Effect of stress relaxation on distortion in additive manufacturing process modeling,” *Addit. Manuf.*, vol. 12, pp. 51–59, Oct. 2016, doi: 10.1016/j.addma.2016.06.011.

[9] D. Veeman, M. D. Vijayakumar, M. K. Subramaniyan, B. Viswanathan, P. Arumugaperumal, and K. Jeevaraj, “Experimental and Finite Element Simulation of Tensile Behavior of Bi-Metallic Structure Fabricated Through Wire Arc Additive Manufacturing,” *Trans. Indian Inst. Met.*, vol. 78, no. 2, p. 54, Jan. 2025, doi: 10.1007/s12666-024-03468-9.

[10] J. Mehnen, J. Ding, H. Lockett, and P. Kazanas, “Design study for wire and arc additive manufacture,” *Int J Prod. Dev.*, vol. 19, pp. 2–20, Jan. 2014, doi: 10.1504/IJPD.2014.060028.

[11] Z. Hu, X. Qin, Y. Li, J. Yuan, and Q. Wu, “Multi-bead overlapping model with varying cross-section profile for robotic GMAW-based additive manufacturing,” *J. Intell. Manuf.*, vol. 31, no. 5, pp. 1133–1147, Jun. 2020, doi: 10.1007/s10845-019-01501-z.

[12] “Analytical Model for Distortion Prediction in Wire + Arc Additive Manufacturing”, Accessed: Feb. 26, 2025. [Online]. Available: https://mrforum.com/product/9781945291890-44/

[13] M. Graf, A. Hälsig, K. Höfer, B. Awiszus, and P. Mayr, “Thermo-Mechanical Modelling of Wire-Arc Additive Manufacturing (WAAM) of Semi-Finished Products,” *Metals*, vol. 8, no. 12, Art. no. 12, Dec. 2018, doi: 10.3390/met8121009.

[14] J. Ding *et al.*, “Thermo-mechanical analysis of Wire and Arc Additive Layer Manufacturing process on large multi-layer parts,” *Comput. Mater. Sci.*, vol. 50, no. 12, pp. 3315–3322, Dec. 2011, doi: 10.1016/j.commatsci.2011.06.023.

[15] J. D. Spencer, P. M. Dickens, and C. M. Wykes, “Rapid prototyping of metal parts by three-dimensional welding,” *Proc. Inst. Mech. Eng. Part B J. Eng. Manuf.*, vol. 212, no. 3, pp. 175–182, Mar. 1998, doi: 10.1243/0954405981515590.

[16] F. W. Brust and D. S. Kim, “8 - Mitigating welding residual stress and distortion,” in *Processes and Mechanisms of Welding Residual Stress and Distortion*, Z. Feng, Ed., in Woodhead Publishing Series in Welding and Other Joining Technologies. , Woodhead Publishing, 2005, pp. 264–294. doi: 10.1533/9781845690939.2.264.

[17] O. Panchenko, I. Kladov, D. Kurushkin, L. Zhabrev, E. Ryl’kov, and M. Zamozdra, “Effect of thermal history on microstructure evolution and mechanical properties in wire arc additive manufacturing of HSLA steel functionally graded components,” *Mater. Sci. Eng. A*, vol. 851, p. 143569, Aug. 2022, doi: 10.1016/j.msea.2022.143569.

[18] I. Gibson, D. Rosen, and B. Stucker, *Additive Manufacturing Technologies: 3D Printing, Rapid Prototyping, and Direct Digital Manufacturing*. New York, NY: Springer, 2015. doi: 10.1007/978-1-4939-2113-3.

[19] D. Ding, Z. Pan, D. Cuiuri, and H. Li, “Wire-feed additive manufacturing of metal components: technologies, developments and future interests,” *Int. J. Adv. Manuf. Technol.*, vol. 81, May 2015, doi: 10.1007/s00170-015-7077-3.

[20] D. Herzog, V. Seyda, E. Wycisk, and C. Emmelmann, “Additive manufacturing of metals,” *Acta Mater.*, vol. 117, pp. 371–392, Sep. 2016, doi: 10.1016/j.actamat.2016.07.019.

[21] S. Patel, Y. Liu, Z. Siddique, and I. Ghamarian, “Metal additive manufacturing: Principles and applications,” *J. Manuf. Process.*, vol. 131, pp. 1179–1201, 2024, doi: 10.1016/j.jmapro.2024.09.101.

[22] D. G. Andrade, T. Tankova, C. Zhu, R. Branco, L. S. da Silva, and D. M. Rodrigues, “Mechanical properties of 3D printed CMT-WAAM 316 LSi stainless steel walls,” *J. Constr. Steel Res.*, vol. 215, p. 108527, Apr. 2024, doi: 10.1016/j.jcsr.2024.108527.

[23] H. Gong, K. Rafi, H. Gu, T. Starr, and B. Stucker, “Analysis of defect generation in Ti–6Al–4V parts made using powder bed fusion additive manufacturing processes,” *Addit. Manuf.*, vol. 1–4, pp. 87–98, Oct. 2014, doi: 10.1016/j.addma.2014.08.002.

[24] D. D’Andrea, “Additive Manufacturing of AISI 316L Stainless Steel: A Review,” *Metals*, vol. 13, no. 8, Art. no. 8, Aug. 2023, doi: 10.3390/met13081370.

[25] S. Kumar, “ER70S-6 welding wire MTC, specification, chemical-mechanical properties,” Material Welding. Accessed: Mar. 01, 2025. [Online]. Available: https://materialwelding.com/er70s-6-welding-wire-mtc-specification-chemical-mechanical-properties/

[26] M. Leino, J. Pekkarinen, and R. Soukka, “The Role of Laser Additive Manufacturing Methods of Metals in Repair, Refurbishment and Remanufacturing – Enabling Circular Economy,” *Phys. Procedia*, vol. 83, pp. 752–760, Jan. 2016, doi: 10.1016/j.phpro.2016.08.077.

[27] B. Xie, J. Xue, and X. Ren, “Wire Arc Deposition Additive Manufacturing and Experimental Study of 316L Stainless Steel by CMT + P Process,” *Metals*, vol. 10, no. 11, Art. no. 11, Nov. 2020, doi: 10.3390/met10111419.

[28] M. Komarasamy, N. Kumar, Z. Tang, R. S. Mishra, and P. K. Liaw, “Effect of Microstructure on the Deformation Mechanism of Friction Stir-Processed $Al_{0.1}$ CoCrFeNi High Entropy Alloy,” *Mater. Res. Lett.*, vol. 3, no. 1, pp. 30–34, Jan. 2015, doi: 10.1080/21663831.2014.958586.

[29] “Strength of Materials Basics and Equations | Mechanics of Materials.” Accessed: Mar. 01, 2025. [Online]. Available: https://www.engineersedge.com/strength_of_materials.htm

[30] N. Connor, “What is Hardening of Metals - Definition,” Material Properties. Accessed: Mar. 01, 2025. [Online]. Available: https://material-properties.org/what-is-hardening-of-metals-definition/

[31] N. Connor, “What is Ductility - Definition,” Material Properties. Accessed: Mar. 01, 2025. [Online]. Available: https://material-properties.org/what-is-ductility-definition/

[32] GIpress, “What is Toughness, Hardness and Strength in a Material?,” Mech Lesson. Accessed: Mar. 01, 2025. [Online]. Available: https://mechlesson.com/toughness-hardness-strength/

[33] S. Sabhadiya, “What Is Elasticity in Materials?- Definition, Examples.” Accessed: Mar. 01, 2025. [Online]. Available: https://www.theengineeringchoice.com/what-is-elasticity/

[34] “Plasticity | Malleability, Elasticity, Ductility | Britannica.” Accessed: Mar. 01, 2025. [Online]. Available: https://www.britannica.com/science/plasticity

[35] “Fracture Toughness Tests: Definition, Purpose, Standards, Process, and Benefits.” Accessed: Mar. 01, 2025. [Online]. Available: https://www.xometry.com/resources/materials/fracture-toughness-tests/

[36] “What is Stiffness in Physics - Definition, Formula, and Types.” Accessed: Mar. 01, 2025. [Online]. Available: https://matmake.com/materials-properties/stiffness.html

[37] “Elastic Modulus vs. Young’s Modulus - What’s the Difference?,” This vs. That. Accessed: Mar. 01, 2025. [Online]. Available: https://thisvsthat.io/elastic-modulus-vs-youngs-modulus

[38] K. Sharma, “Yield Strength: Formula, Curve, Example, Applications.” Accessed: Mar. 01, 2025. [Online]. Available: https://scienceinfo.com/yield-strength-formula-curve-example-applications/

[39] G. O. Barrionuevo, I. La Fé-Perdomo, E. Cáceres-Brito, and W. Navas-Pinto, “TENSILE/COMPRESSIVE RESPONSE OF 316L STAINLESS STEEL FABRICATED BY ADDITIVE MANUFACTURING,” *Ingenius Rev. Cienc. Tecnol.*, no. 31, pp. 9–18, Jun. 2024, doi: 10.17163/ings.n31.2024.01.

[40] K. Sharma, “Ultimate Tensile Strength (UTS): Formula, Application, Advantages.” Accessed: Mar. 01, 2025. [Online]. Available: https://scienceinfo.com/ultimate-tensile-strength-uts-formula-application-advantages/

[41] H. Jamal, “True Stress & True Strain | Engineering Stress-Strain.” Accessed: Mar. 01, 2025. [Online]. Available: https://www.aboutcivil.org/true-stress-true-strain-engineering-stress-strain.html

[42] H. Geng, J. Li, J. Xiong, X. Lin, and F. Zhang, “Optimization of wire feed for GTAW based additive manufacturing,” *J. Mater. Process. Technol.*, vol. 243, pp. 40–47, May 2017, doi: 10.1016/j.jmatprotec.2016.11.027.

[43] P. A. Colegrove *et al.*, “Microstructure and residual stress improvement in wire and arc additively manufactured parts through high-pressure rolling,” *J. Mater. Process. Technol.*, vol. 213, no. 10, pp. 1782–1791, Oct. 2013, doi: 10.1016/j.jmatprotec.2013.04.012.

[44] U. Gürol, B. Turgut, H. Kumek, S. Dilibal, and M. Koçak, “Fabrication and Characterization of Wire Arc Additively Manufactured Ferritic-Austenitic Bimetallic Structure,” *Met. Mater. Int.*, vol. 30, no. 5, pp. 1342–1355, May 2024, doi: 10.1007/s12540-023-01568-7.

[45] G. Marinelli, F. Martina, S. Ganguly, and S. Williams, “Development of Wire + Arc additive manufacture for the production of large-scale unalloyed tungsten components,” *Int. J. Refract. Met. Hard Mater.*, vol. 82, pp. 329–335, Aug. 2019, doi: 10.1016/j.ijrmhm.2019.05.009.

8 Appendix:

This appendix provides a brief explanation of the simulation modeling procedure followed in Abaqus, demonstrated here for a single tensile specimen. The same method can be applied to all other specimens. The modeling process involves eight main steps, starting from the creation of the 3D model to the analysis of results. The first step is carried out in the part module, where the 3D geometry of the specimen is created. In this study, the part being modeled is a tensile specimen. At this stage, the part appears white in color, as shown in Figure a, indicating that no material properties have been assigned yet. Moving to the next step, which takes place in the property module, the material definitions are created by specifying elastic, plastic, and damage behavior as required. After defining the material, it is assigned to the part. Once the material assignment is complete, the color of the 3D model changes—typically to green—indicating that the section has been properly applied, as seen in Figure b. This marks the successful transition from geometry creation to the initial stage of material setup, forming the basis for the subsequent modules in the simulation workflow.

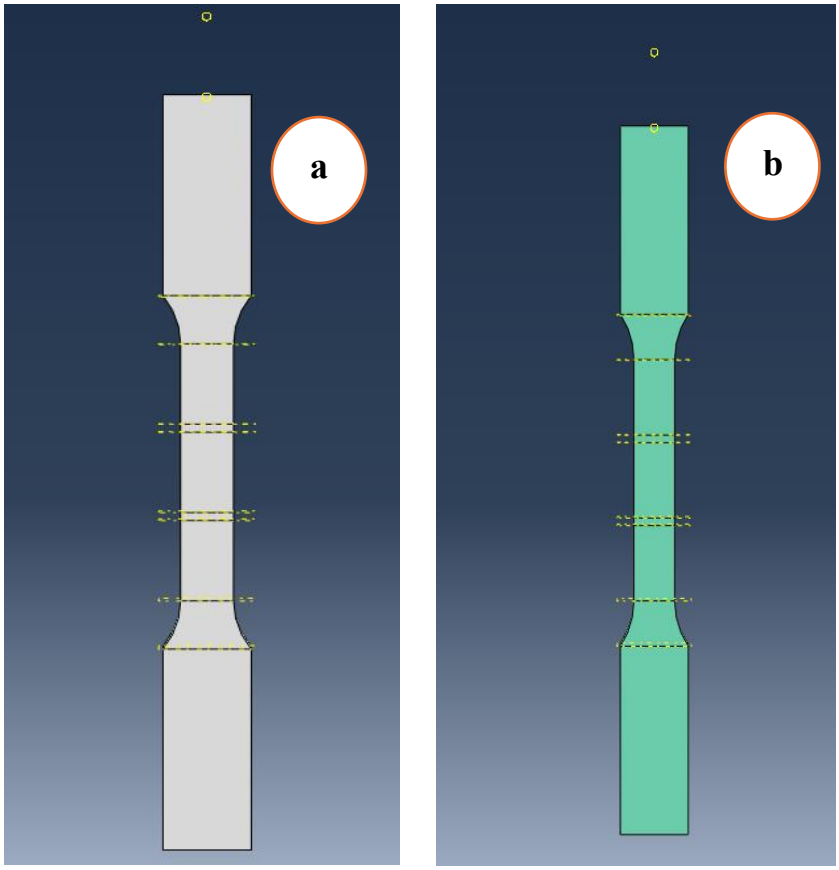

The third module in the Abaqus simulation process is the assembly module, which in this case does not require significant modifications since the model consists of a single part and does not involve multiple components. The fourth module, known as the step module, is one of the most important and sensitive stages in the simulation. It involves the use of the step manager, where incrementation settings are defined. These settings control how the solver progresses through the analysis, and incorrect values can lead to non-convergence, causing the simulation to fail or abort. Therefore, it is essential to define them carefully to ensure numerical stability. Additionally, this module is where field outputs and history outputs are specified, which determine the simulation results and parameters that will be available for post-processing and analysis. The next module is interaction,

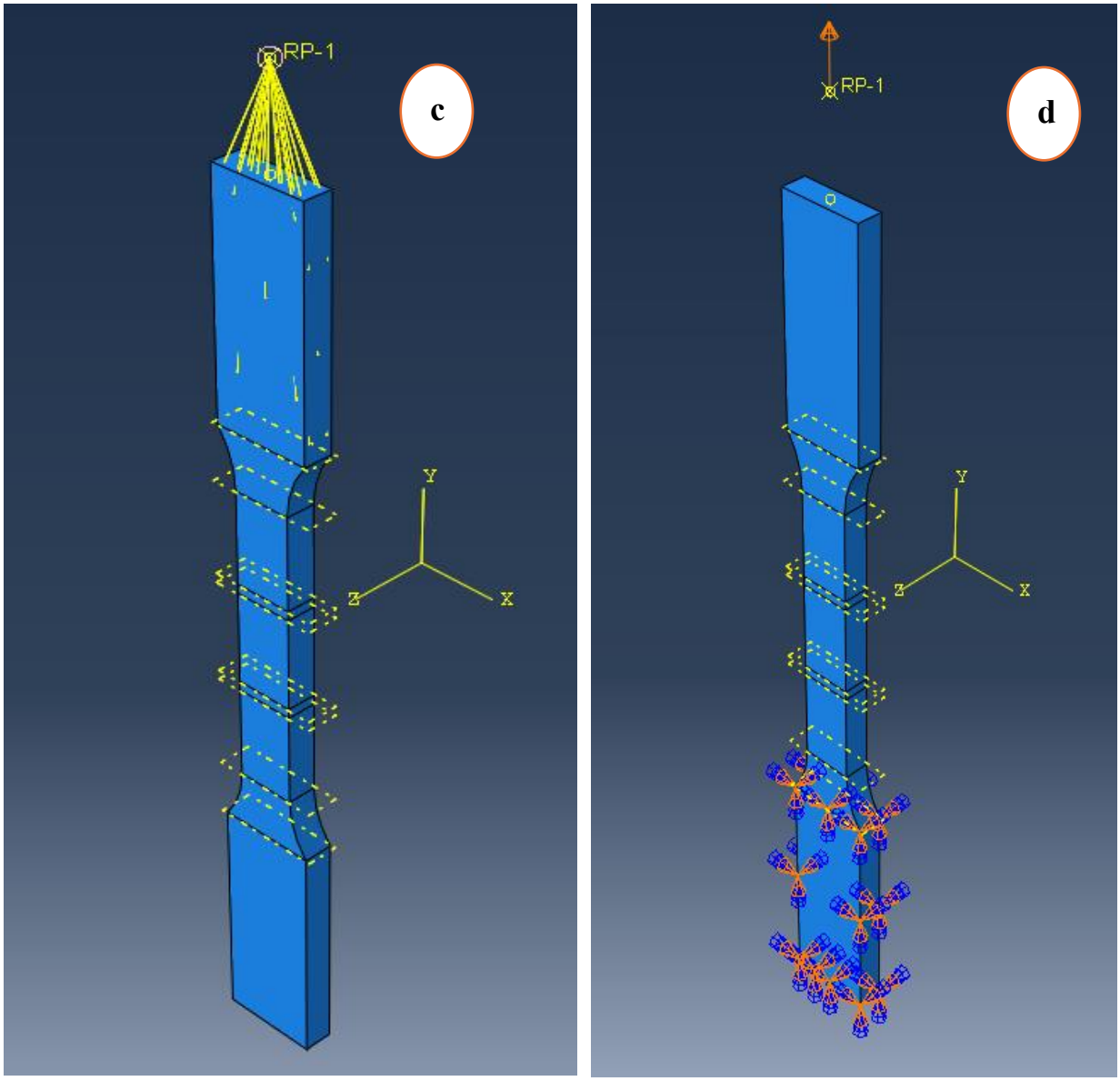

where the coupling conditions of the model are defined. Specifically, in this study, the upper end of the tensile specimen is kinematically coupled to a reference point, which acts as the location where the external load is applied during the simulation as shown in figure c. This coupling ensures that the load is evenly distributed across the specimen's surface.

Following the interaction module, the next stage is the load module, which is also of significant importance in the simulation process. In this module, boundary conditions and external loads are applied to the model. For the tensile specimen used in this study, the lower end is fully constrained using an encastre boundary condition, meaning all degrees of freedom are fixed at that end. At the same time, a displacement load is applied to the reference point at the upper end of the specimen. This load is applied in the Y-direction and is defined as a prescribed displacement of 15 mm. This setup simulates a tensile test by stretching the specimen upward under controlled displacement, allowing for accurate analysis of stress-strain behavior throughout the gauge section. It can be seen in figure d of appendix.

The next module in the simulation workflow is the mesh module, where the finite element mesh is generated for the model. In this study, both global and local meshing strategies were employed to balance computational efficiency with accuracy. A global mesh with relatively coarser elements was applied to the less critical regions of the specimen where stress gradients are minimal. In contrast, local mesh refinement was used in the gauge area, the region where mechanical behavior is of primary interest—and more specifically in the transition zone between the two materials shown in figure e and f. This zone is expected to experience complex stress distribution, and therefore a finer mesh was essential to accurately capture the stress concentration and deformation patterns in this critical region.

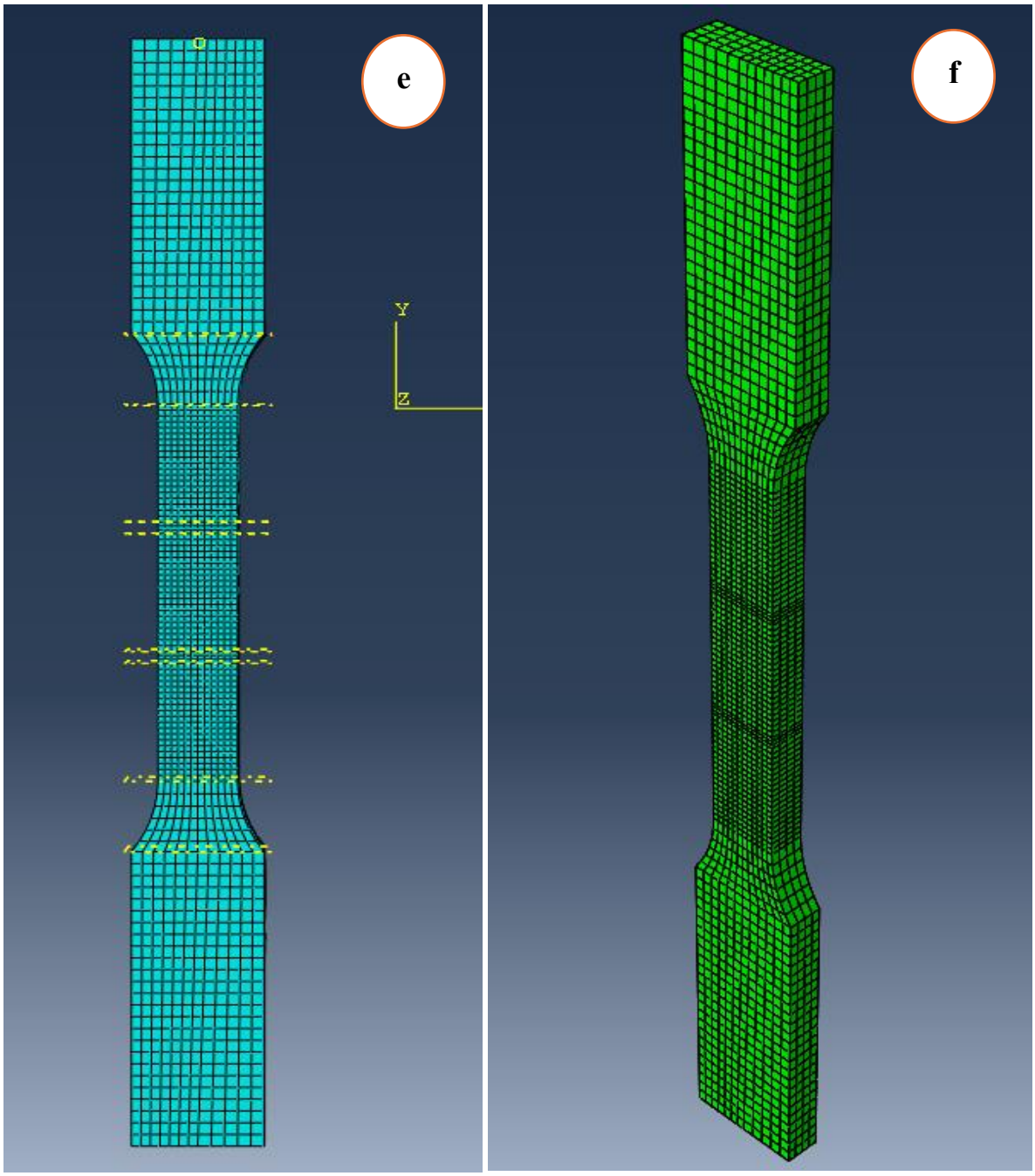

The final steps in the simulation process include the **optimization module** and **job submission**. In the optimization module, although not always required, users have the option to perform design studies or refine parameters to improve model efficiency or performance. Once all setup steps are complete, the model is submitted through the **job module**, where a new job is created and the analysis is launched. The simulation then runs based on the defined settings and may take varying

amounts of time depending on model complexity, mesh density, and computational resources. Upon successful completion, the results can be viewed in the **visualization module**, where outputs such as stress distribution, strain fields, and deformation shapes can be examined. This module provides graphical and numerical insights that are critical for interpreting the mechanical response of the specimen under the applied loading conditions. Results of von mises stress propagation and failure can be seen in figure g,h,i and j.

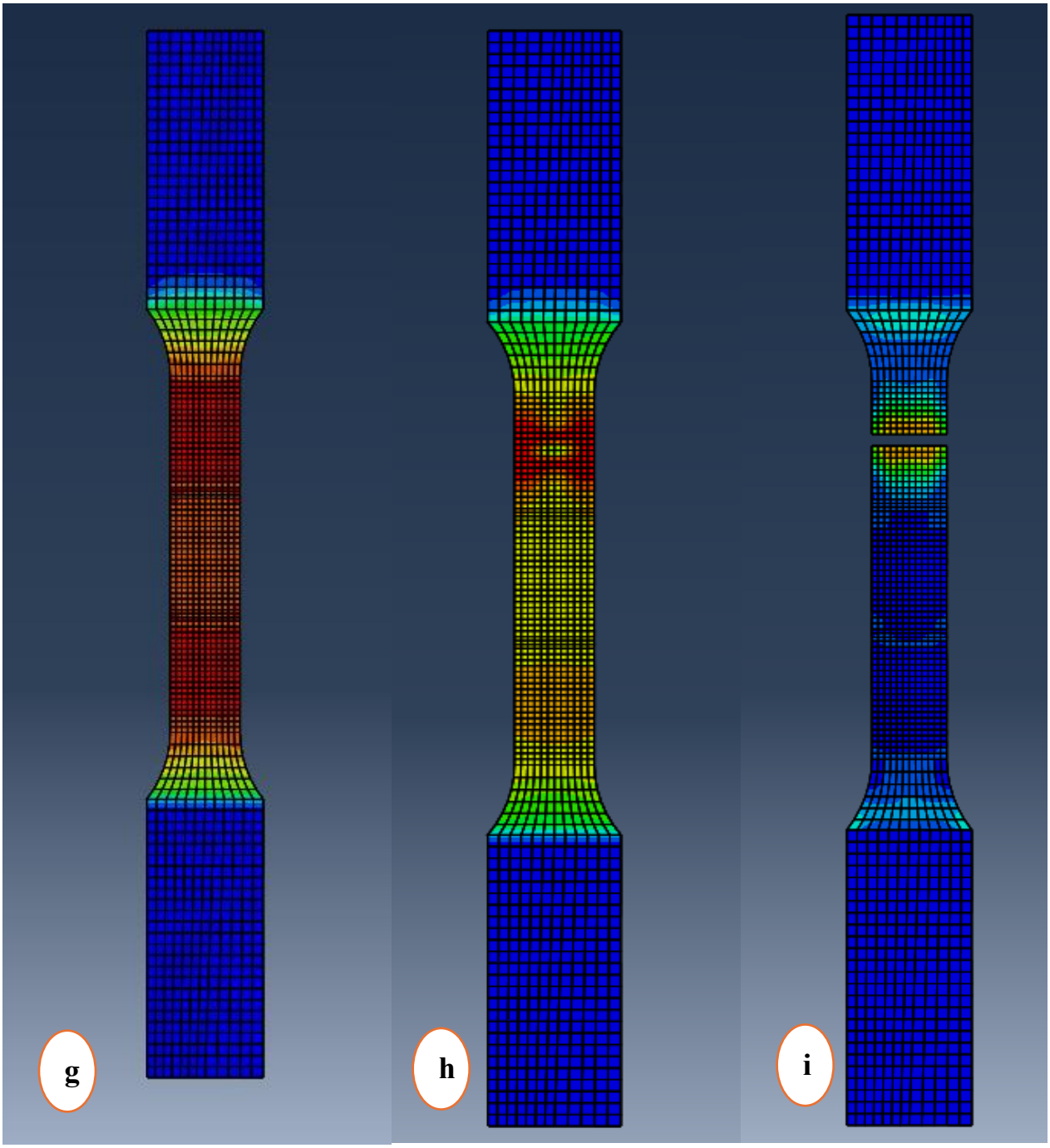

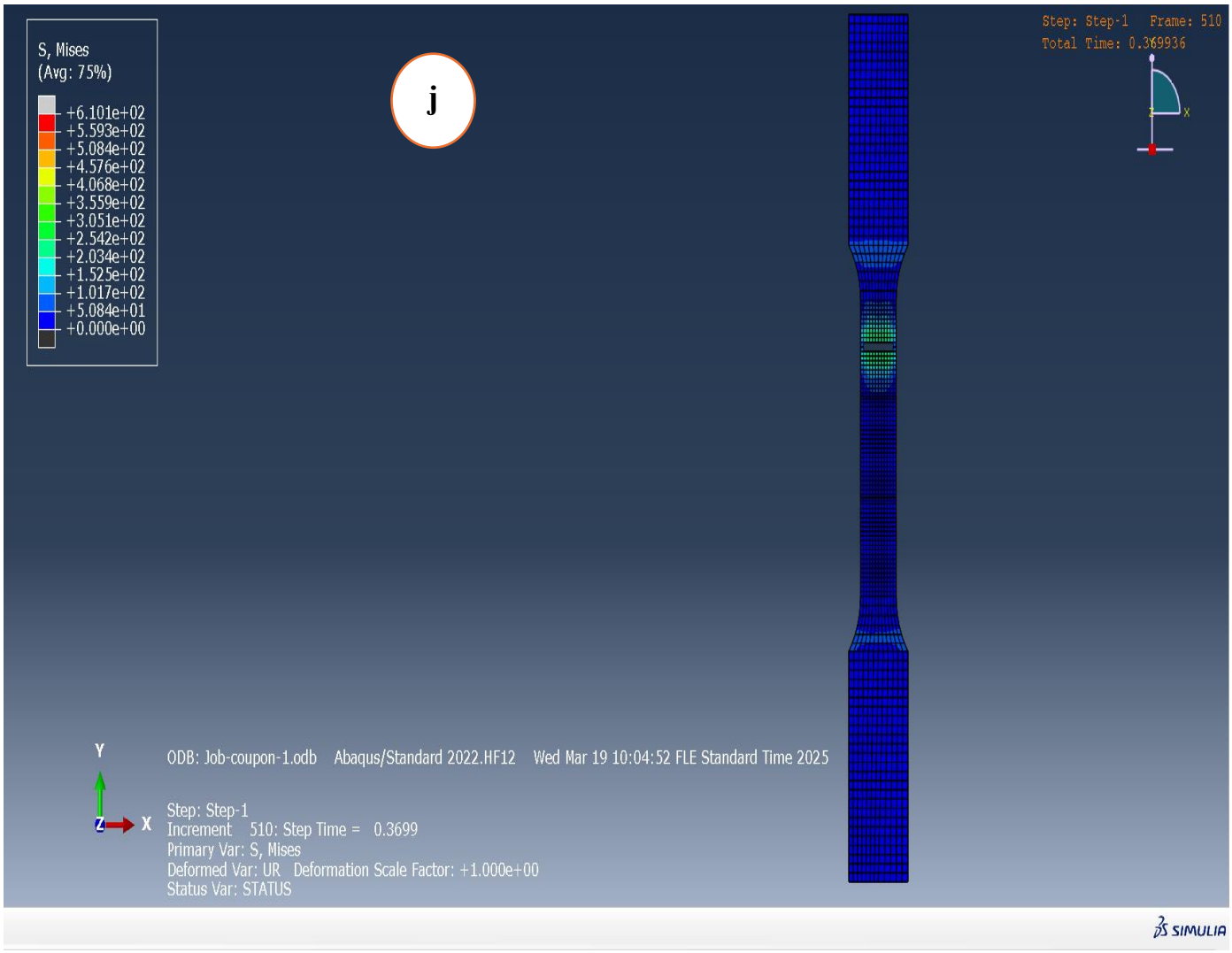
S, Mises
(Avg: 75%)
+6.101e+02
+5.593e+02
+5.084e+02
+4.576e+02
+4.068e+02
+3.559e+02
+3.051e+02
+2.542e+02
+2.034e+02
+1.525e+02
+1.017e+02
+5.084e+01
+0.000e+00
j
Step: Step-1 Frame: 510
Total Time: 0.3699936
Y
X
ODB: Job-coupon-1.odb Abaqus/Standard 2022.HF12 Wed Mar 19 10:04:52 FLE Standard Time 2025
Step: Step-1
Increment 510: Step Time = 0.3699
Primary Var: S, Mises
Deformed Var: UR Deformation Scale Factor: +1.000e+00
Status Var: STATUS
SIMULIA